Transcriptional changes consistent with altered neuronal differentiation, angiogenesis, and tumor plasticity induced in human subpallial telencephalic organoid-glioblastoma chimeras.

Simone Chiola[1], Jingye Yang[2,5], H M Arif Ullah[1], Kandy Napan[1], Qiju Huang[1], Nicholas Gamboa[2,5], Osama Youssef[2,5], Howard Colman[2,5], *Samuel H. Cheshier[2,5,7], *Alex Shcheglovitov[1,3,4,5,6]

[1]Department of Neurobiology, University of Utah

[2]Division of Pediatric Neurosurgery, Department of Neurosurgery, University of Utah

[3]Departments of Psychiatry, University of Utah

[4]Departments of Biomedical Engineering, University of Utah

[5]Huntsman Cancer Institute

[6]Clinical and Translational Research Core, Utah Clinical and Translational Research Institute

[7]Intermountain Primary Children's Hospital

*The Co-senior, co-corresponding authors contributed equally to this work.

Correspondence: alexsh@neuro.utah.edu (Alex Shcheglovitov) or samuel.cheshier@hci.utah.edu (Samuel Cheshier)

Abstract

Glioblastoma multiforme (GBM) is one of the most aggressive and therapy-resistant brain tumors prevalent in both adults and children. Despite extensive research to understand GBM pathology, it remains unclear how neural cells in the human brain interact with GBM cells to support their brain propagation and therapy resistance and whether GBM cells exert any influence on the properties of human neural cells. In this study, we co-culture human stem cell-derived subpallial telencephalic organoids with patient-derived proneural or mesenchymal GBM spheroids to investigate their reciprocal interactions. We show that both proneural and mesenchymal GBM spheroids readily fuse and propagate with human organoids, forming organoid-GBM chimeras, without the need for exogenous growth factors. GBM cells within the chimeras adapt by modulating gene expression profiles consistent with diminished proliferation, heightened hypoxia, increased angiogenesis, and proneural-to-mesenchymal transition in proneural GBM. Both proneural or mesenchymal GBMs also exert an impact on the properties of neural cells in the chimeras, leading to the suppression of neuronal genes and an upregulation expression of genes associated with hypoxia and angiogenesis. Collectively, this study identifies specific genes and molecular pathways that can be altered in GBM and neural cells by reciprocal interactions in a human developing brain-like environment for an increased understanding of GBM pathology and future therapy development.

Keywords: glioblastoma multiforme, GBM, human stem cell-derived organoids, tumor signaling

Introduction

Glioblastoma (GBM, WHO Grade IV IDH-wildtype diffuse astrocytic glioma) is one of the deadliest primary brain tumors affecting individuals of all ages (Brat et al. 2018; Ostrom et al. 2019; Louis et al. 2021). Although GBM has been extensively investigated in xenograft animal models (Bhat et al. 2013; Osswald et al. 2015; Venkatesh et al. 2015, 2017; Venkataramani et al. 2019) and many previous clinical trials (Tan et al. 2020), no effective therapies exist for patients (Le Rhun et al. 2019). Unfortunately, patients diagnosed with GBM survive on average for only 12-24 months after the initial diagnosis (Tykocki and Eltayeb 2018). It is believed that inter- and intra-tumoral heterogeneity (Patel et al. 2014; Hu et al. 2017; Skaga et al. 2019; Wenger et al. 2019) as well as the brain microenvironment (Venkatesh et al. 2015, 2019; Monje et al. 2020) may be the factors influencing clinical trial outcomes.

GBM heterogeneity has been characterized according to histopathological tumor appearance, marker genes, and single-cell RNA sequencing (scRNA-seq) (Huse et al. 2011; Neftel et al. 2019; Bhaduri, di Lullo, et al. 2020; Couturier et al. 2020a). The GBM molecular subtypes based on genomic and transcriptional profiling include: pro-neural (PN), neural (N), classical (C), and mesenchymal (MES) (Balasubramaniyan et al., 2015; Bhat et al., 2013; Phillips et al., 2006). However, multiple molecular subtypes can coexist within a tumor at different relative preponderance and change identity over time (Sottoriva et al. 2013; Patel et al. 2014; Wang et al. 2018). The scRNA-seq profiling of GBM cells has allowed tumor cell classification based on the expression of cell identity markers into mesenchymal (MES)-, oligodendrocyte progenitor (OPC)-, astrocyte (AC)-, and neural

70 progenitor cell (NPC)-like tumor cells (Neftel et al. 2019). Specific genetic aberrations
71 primarily drove this classification, but the knowledge of genetic aberrations remains
72 insufficient to predict tumor responses to specific treatments (Jacob et al. 2020).
73
74 The effects of the brain microenvironment on GBM cells have recently been
75 investigated using human stem cell-derived brain organoids GBM (Bian et al. 2018a; da
76 Silva et al. 2018a; Ogawa et al. 2018a; Linkous et al. 2019a; Pine et al. 2020a; Tang et
77 al. 2020). Organoids recapitulate many important aspects of early human brain
78 development (Eiraku et al. 2008; Mariani et al. 2012; Kadoshimaa et al. 2013; Lancaster
79 et al. 2013; Pasca et al. 2015; Qian et al. 2016), including organization and the presence
80 of primate-specific neural stem cells, [i.e., outer radial glia (oRG)] (Kadoshimaa et al.
81 2013; Qian et al. 2016; Watanabe et al. 2017), that have been associated with the
82 expansion of the human cerebral cortex (Rakic 2009; Lui et al. 2011) and disorders such
83 as lissencephaly (Bershteyn et al. 2017) and GBM (Bhaduri, di Lullo, et al. 2020). Brain
84 organoids and GBM cells grown in suspension in defined media (GBM spheroids) can
85 efficiently assemble into organoid-GBM chimeras. Tumor cells can invade organoids and
86 proliferate without requiring exogenous growth factors (Lee et al. 2006a). Importantly, it
87 has also been demonstrated that GBM cells in chimeras possessed increased resistance
88 to irradiation and chemotherapy (Linkous et al. 2019a) and maintained single-cell gene
89 expression signatures reminiscent of those detected in the resected primary parental
90 tumors (Pine et al. 2020a). However, the molecular signaling pathways activated in GBM
91 cells by fusion with organoids remain unknown. In addition, it is still unclear whether and
92 how tumor cells influence the development of normal neural cells in organoids.

93

94 In this study, we demonstrated that mesenchymal and pro-neural GBM spheroids
95 could be efficiently propagated without the tumor-required growth factors when fused with
96 telencephalic organoids consisting of subpallial neural progenitors and GABAergic
97 inhibitory neurons. We used single-cell RNA sequencing to investigate gene expression
98 profiles in single cells obtained from GBM spheroids, organoids, and organoid-GBM
99 chimeras to gain insights into the molecular pathways associated with tumor growth in
100 the human brain-like environment. We found that both mesenchymal and pro-neural
101 GBMs suppressed the gene expression network associated with telencephalic
102 development and neuronal differentiation in organoids. On the other hand, organoids
103 suppressed the expression levels of mitochondrial and proliferation genes and
104 upregulated those associated with cell communication, neuronal activity, angiogenesis,
105 and hypoxia in GBMs. Overall, this study describes genes and signaling pathways
106 associated with tumor growth and propagation in the organoid-GBM chimeras. It also
107 provides insights into the effects of GBM tumors on normal human brain development.

108

109 **RESULTS**

110 **Multiple neural and mesenchymal cell types coexist in patient-derived GBM**
111 **spheroids**

112 Patient-derived GBM spheroids have been used as *in vitro* models for studying the
113 cellular and molecular changes in human brain tumors and for drug discovery (Lee et al.
114 2006b; Ledur et al. 2017). However, the propagation and survival of GBM tumors *in vitro*
115 are often dependent on the presence of exogenous epithelial growth factor and basic

116 fibroblast growth factor (EGF and FGF, respectively) in the culture media (Lee et al.
117 2006b). EGF and FGF are well-known morphogens that can influence cell identity, gene
118 expression profile, and resistance to anti-cancer treatments (Szymczyk et al. 2021). We
119 investigated the properties of mesenchymal (MS) and proneural (PN) GBM spheroids
120 obtained from patient-derived brain tumors using scRNA-seq (**Fig. 1A-B**) (Bhat et al.
121 2013; Balasubramaniyan et al. 2015). Neither MS- or PN-GBM spheroids survived for
122 more than 12 days without EGF/FGF *in vitro* (**Fig. 1C-F**), which is consistent with the
123 results of the previous study on these tumors (Bhat et al. 2013). However, both PN-
124 (GBM11) and MS (GBM20) spheroids were robustly propagated in the presence of EGF
125 and FGF (**Fig. 1C-F**).

126 To compare and contrast the cellular composition in PN- (GBM11) and MS-
127 (GBM20) spheroids, we collected single cells from multiple spheroids propagated in the
128 presence of exogenous EGF (20 ng/mL) and FGF (20 ng/mL) for 12-14 days *in vitro* (**Fig.**
129 **1A-B**). We found substantially different cell compositions in these spheroids based on
130 non-supervised cell clustering and expression levels of cell cluster-specific genes (**Fig.**
131 **1G-I**, **Supplementary Fig. 1,** and **Supplementary Dataset 1**). PN-GBM spheroids (8,421
132 cells analyzed) were primarily distributed between 6 cell clusters (**Fig. 1J**) and consisted
133 of cells expressing pro-neural cell markers, including *ASCL1*, *OLIG2*, and *NCAM1* (**Fig.**
134 **1K**). MS-GBM spheroids (8,658 cells analyzed) were enriched with cells expressing
135 mesenchymal cell markers, including *FOXC1, MDK*, and *TGFBI* (**Fig. 1K**), and distributed
136 to a different set of 6 cell clusters (**Fig. 1J**). Both types of spheroids demonstrated an
137 elevated expression of GBM stem cell markers *CD109* and *MYC*, PN-GBM marker *DLL3*,
138 and MS-GBM markers *TIMP1* and *CD44* (Bhat et al. 2013)(**Fig. 1K**). Interestingly, tumor

139 cells in both MS- and PN-GBM spheroids demonstrated increased expression of genes
140 associated with subpallial telencephalic cell identities, including *FOXG1*, *SOX3*, *DLX1/2*,
141 and *ASCL1* (**Supplementary Fig. 2**), suggesting the subpallial developmental origin of
142 these tumors (Couturier et al. 2020b).
143
144 To further characterize the cell composition of MS- and PN-GBM spheroids, we
145 assessed the identities of tumor spheroid cells using the average expression of gene
146 signatures associated with different cellular states detected in primary GBMs, such as
147 NPC-, AC-, OPC- and MES-like cell states (Neftel et al. 2019). This analysis revealed that
148 PN-GBM spheroids primarily consisted of AC-like cells (88.6%) with smaller fractions of
149 MES- (10.1%), NPC- (1.1%), and OPC-like cells (0.27%) (**Fig. 1L**). In contrast, MS-GBM
150 spheroids were composed of MES-like cells (99.33%) with minor fractions of NPC- and
151 AC- (0.46% and 0.13%, respectively) and no OPC-like cells (**Fig. 1L**). These findings
152 highlight the distinct cellular composition and gene-expression profiles of PN-GBM and
153 MS-GBM spheroids, underscoring their unique identities. However, despite these
154 differences, the in vitro growth of both PN-GBM and MS-GBM spheroids depended on
155 the addition of exogenous EGF and FGF to the culture medium. Since EGF and FGF are
156 potent morphogens that regulate cell identities and proliferation, we next investigated
157 whether GBM spheroids can be propagated without growth factors in co-culture with
158 human stem cell-derived telencephalic organoids to mimic a human-brain-like
159 microenvironment of GBM tumors in the developing brain.
160
161

162 **Generation and characterization of hPSC-derived subpallial telencephalic**
163 **organoids from isolated single neural rosettes**

164 We previously demonstrated that telencephalic organoids generated from isolated
165 human stem cell-derived single neural rosettes (SNR) consist of pallial and subpallial
166 neural progenitors (NPs) and both excitatory and inhibitory neurons and show
167 reproducible cellular composition and organization (Wang et al. 2022). To create a
168 microenvironment appropriate for co-culturing GBMs that exhibit the expression of
169 subpallial telencephalic markers, including FOXG1, NKX2.2, SOX6, and DLX1
170 (**Supplementary Fig. 2**), we adapted the protocol to generate subpallial telencephalic
171 organoids from SNRs (**Fig. 2, Supplementary Fig. 3,** and **Supplementary Dataset 2)**.
172 SNR-derived subpallial organoids were generated in three separate batches from two
173 different human pluripotent stem cells (hPSC) lines: embryonic stem cell (ESC) line H9
174 and control induced pluripotent stem cell (iPSC) line (AICS-0054-09), in which
175 membrane-tagged RFP was inserted into the AAVS1 locus under the control of the
176 CAGGS promoter (RFP-iPSC). Consistent with our previous observations (Wang et al.
177 2022), we observed that SNR-derived organoids increased in size over time and
178 maintained a single visible lumen (**Fig. 2A**). At about two weeks post-rosette isolation,
179 SNR-derived subpallial organoids reached the size of 0.15 - 0.3 mm^2 (**Fig. 2B**). To
180 characterize the cellular composition of these organoids, we performed scRNA-seq and
181 analysis on 17,893 cells collected from 12 organoids produced in 3 separate
182 differentiation batches from H9 and iPSC-RFP lines, 3-9 organoids (2,190-15,703 cells)
183 per batch (**Fig. 2C**). The cellular compositions of dissociated organoids were reproducible
184 across differentiation batches (**Fig. 2C-E**). The majority of cells within the SNR-derived

185 organoids exhibited expression of the telencephalic marker FOXG1 (**Fig. 2G-H**). The cells
186 in clusters 3 and 11 displayed the expression of early subpallial neural progenitor (NP)
187 markers, including *NES, SOX2, NKX2-1, GSX2*, and *NKX2-1*, indicating their identity as
188 subpallial telencephalic NPs (**Fig. 2F-H**). Conversely, clusters 7 and 9 exhibited
189 heightened expression levels of intermediate subpallial NP markers such as *ASCL1,*
190 *DLX1/2*, and *LHX6*, identifying them as subpallial telencephalic intermediate progenitors
191 (IPs) (**Fig. 2F-H**). The cells in the remaining clusters (0-2, 4-6, and 8) were characterized
192 by the expression of markers associated with GABAergic neurons, including *STMN2,*
193 *GAD1*, and *GAD2*, supporting their classification as inhibitory neurons (**Fig. 2F-H**).
194 Importantly, we detected no or very low expression of the pallial telencephalic NP and IP,
195 and glutamatergic cortical neuron markers, including *PAX6, EOMES, SLC17A7* and
196 *TBR1* (**Fig. 2G-H** and **Supplementary Fig. 3**), which is consistent with the subpallial
197 telencephalic identities of cells in these organoids. These results suggest that subpallial
198 telencephalic organoids can be reproducibly generated from SNRs.
199

200 **Subpallial telencephalic organoids support *in vitro* propagation of GBM**
201 **spheroids without exogenous growth factors**

202 We assembled organoid-GBM chimeras by placing single MS- or PN-GBM
203 spheroids together in the same well with a 1-month-old subpallial SNR-derived organoid
204 (**Fig. 3A**). Both MS-GBM and PN-GBM spheroids exhibited 100% fusion rate with the
205 organoids, resulting in the formation of organoid-GBM chimeras that demonstrated a
206 progressive increase in size over time (**Fig. 3B and Supplementary Fig. 4**). This is
207 consistent with the results of the previous studies on cerebral and cortical organoids and

208 GBM spheroids (Bian et al. 2018b; da Silva et al. 2018b; Ogawa et al. 2018b; Linkous et
209 al. 2019b; Pine et al. 2020b; Tang et al. 2020). Since cells in MS-GBM spheroids
210 ubiquitously expressed GFP and SNR-derived organoids produced from the iPSC-RFP
211 line expressed membrane-tagged RFP, we used this combination to investigate the
212 relative distributions of tumor (GFP-expressing cells) and normal neural cells (RFP-
213 expressing cells) in chimeras (**Fig. 3C-D** and **Supplementary Movie**). We observed that
214 both tumor cells and normal cells exhibited efficient infiltration into the organoid and tumor
215 tissue, respectively. These results suggest that human subpallial telencephalic organoids
216 provide essential factors that sustain the survival and propagation of GBMs *in vitro*,
217 without the reliance on exogenous EGF and FGF.
218
219 To gain insights into the cellular composition of organoid-GBM chimeras and the
220 molecular pathways altered in tumor cells by organoids, we performed single-cell RNA
221 sequencing and non-supervised clustering analysis on 39,554 cells collected from 12 MS-
222 and 6 PN-GBM-organoid chimeras that we generated in five separate differentiation
223 batches (**Fig. 3E-G** and **Supplementary Dataset 3**). The analysis revealed similar
224 compositions of cells in MS-GBM-organoid chimeras across 3 differentiation batches and
225 in PN-GBM-organoid chimeras across 2 differentiation batches (**Fig. 3G**). However, the
226 composition of cells in MS- GBM-organoid chimeras remained significantly different as
227 compared to PN-GBM-organoid chimeras (**Fig. 3G**). In addition, analysis of gene
228 expression profiles in the chimeras revealed distinct differences between GBM and
229 organoid cells; therefore, these cells were largely distributed to different cell clusters (**Fig.
230 3H**). Notably, the distinction between PN-GBM and MS-GBM cells based on their gene

231 expression profiles (tumor clusters) (**Fig. 3H**) was less apparent within chimeras
232 compared to the separation observed in spheroids (**Fig. 1J**), suggesting that the organoid
233 microenvironment likely influences the gene expression profiles of the tumor cells.
234
235 Consistent with this idea, we found that the composition of tumor cells in PN-GBM
236 chimeras underwent significant changes, with a notable shift towards "MES-like" cell
237 states (AC: 25.2%, MES: 73.6%, NPC: 1.1%, and OPC: 0% of all cells) (**Fig. 3I**), in
238 contrast to PN-GBM spheroids (**Fig. 1L**). However, the cell composition in MS-GBM
239 chimeras (MES: 99.12% and NPC: 0.84% of all cells) (**Fig. 3I**) remained similar to that
240 observed in MS-GBM spheroids (**Fig. 1L**). This shift in composition was accompanied by
241 the up-regulated expression of several MES-signature genes (Neftel et al., 2019),
242 including *ATF3, CDKN1A, NAMPT, DDIT3, GSN,* and *ENO2* (**Fig. 3J**), and down-
243 regulation of AC-signature genes, such as *MLC1, NDRG2, MT3, SLC1A3, PRCP,* and
244 *SPARC* (**Fig. 3K**), in PN-GBM chimeras. This result supports the notion that tumor cell
245 identities are plastic and can be significantly influenced by the surrounding
246 microenvironment (Lee et al. 2008; Berezovsky et al. 2014; Neftel et al. 2019; Jung et al.
247 2021; Lauko et al. 2022; Yabo et al. 2022). Moreover, it implies that human brain-like
248 conditions provided by subpallial telencephalic organoids facilitate the adoption of the
249 MES-like gene expression signature by PN-GBMs. The MES-like GBM state is known to
250 be associated with therapy resistance and poor prognosis for survival (Colman et al.
251 2010; Bhat et al. 2013).
252

253 **Tumor cells in organoids-GBM-chimeras undergo transcriptional changes**
254 **consistent with altered glycolysis, quiescence, invasiveness, and angiogenesis.**

255 To understand the molecular changes occurring in tumor cells within chimeras, we
256 compared the gene expression profiles of tumor cells from chimeras and those from
257 spheroids (**Fig. 4A**). Non-supervised clustering analysis was performed on all cells
258 collected from GBM spheroids, consisting of 8,658 cells from MS-GBM spheroids and
259 8,421 cells from PN-GBM spheroids, as well as non-RFP-expressing tumor cells collected
260 from chimeras containing RFP-expressing organoids, including 7,797 cells from MS-GBM
261 chimeras and 4,528 cells from PN-GBM chimeras (**Fig. 4B-C** and **Supplementary**
262 **Dataset 4**). This analysis revealed that there were still substantial differences in the gene
263 expression profiles between PN and MS tumor cells from both chimeras and spheroids.
264 Indeed, PN tumor cells from chimeras exhibited elevated expression of pro-neural genes,
265 including *OLIG2, ASCL1*, and *NCAM1* (**Supplementary Fig. 5**). In contrast, MS-GBM
266 cells from chimeras showed increased expression of genes associated with
267 mesenchymal cell states, such as *FOXC1, MDK*, and *FGFB1* (**Supplementary Fig. 5**).
268 Consequently, PN tumor cells and MS tumor cells from both spheroids and chimeras were
269 largely distributed to distinct cell clusters (**Fig. 4D-G**). However, the composition of cell
270 clusters and the proportion of cells in these clusters were similar between PN -GBMs or
271 MS-GBMs from chimeras and PN-GBMs or MS-GBMs from spheroids, respectively (**Fig.**
272 **4G**). Thus, PN tumor cells from spheroids were pooled with PN tumor cells from chimeras,
273 and MS tumor cells from spheroids were pooled with MS tumor cells from chimeras for
274 the identification of differentially expressed genes and molecular programs (**Fig. 4 H-I** and
275 **Supplementary Datasets 5-6**). This analysis revealed that several mitochondrial genes,

276 including those encoding oxidative phosphorylation system (OXPHOS) complexes (*MT-*
277 *ATP6*, *MT-C03*, *MT-CYB, MT-ND1, and MT-ND3)* and mitochondrial isomerase *EC1,*
278 were significantly downregulated in both PN and MS tumor cells from chimeras as
279 compared to those from spheroids (**Fig. 4H-J**). These changes are consistent with the
280 idea that GBM cells in chimeras more readily utilize glycolysis for energy metabolism
281 outside the mitochondria than GBM cells in spheroids. Indeed, several genes associated
282 with glycolysis, including *DDIT3*, *PGK1*, and *NDRG1,* and mitophagy*,* including *BNIP3*
283 and *BNIP3L,* were upregulated in GBM cells from chimeras (**Fig. 4K**). Other genes
284 upregulated in chimeras were activity-regulated immediate early genes *EGR1*, *IER2*, and
285 *FOS* (Sun and Lin 2016)*,* angiogenesis gene *VEGFA* (Bao et al. 2006), tumor
286 invasiveness and metastases gene *MALAT1* (Venkataramani et al. 2022), and hypoxia
287 and oxidative stress genes *BNIP3L, FAM162A, BNIP3, HILPDA, PGK1, NDRG1, VEGFA,*
288 and *DDIT3* (**Fig. 4K**). These results suggest that GBM cells exposed to a human brain-
289 like environment adapt to it by altering the expression levels of multiple genes associated
290 with cell metabolism. The observed changes may contribute to increased quiescence of
291 tumor cells in chimeras based on increased glycolysis (Zhou et al. 2011; Strickland and
292 Stoll 2017), invasiveness, and vascularization.
293
294 To understand the effects of the organoid microenvironment on the proliferation/
295 quiescence of GBM cells in chimeras, we investigated the expression levels of marker
296 genes associated with mitosis and cell cycle (Xie et al. 2022). We found dramatically
297 reduced expression levels of the mitosis and S-Phase signature genes in both MS- and
298 PN-GBM cells in the chimeras compared to spheroids (**Fig. 4L-M**). These results suggest

299 that GBM cells in chimeras are less proliferative and possibly more quiescent than those
300 in spheroids. However, we found that only certain glioblastoma quiescence signature
301 genes [“cancer stem cell signature” (Xie et al. 2022)] were upregulated in PN-GBM (16
302 out of 118) and MS-GBM (2 out of 118) cells in chimeras (**Fig. 4N**). Interestingly, among
303 the genes upregulated in PN-GBMs, some were outer radial glia (oRG) marker genes,
304 such as *CLU*, *HES1*, *GFAP*, *CRYAB*, and *FAM107A* (Pollen et al. 2015). Elevated
305 expression of oRG genes was identified in a population of oRG-like cancer stem cells in
306 primary glioblastoma tumors (Bhaduri, di Lullo, et al. 2020). Together, these results
307 suggest that GBM cells exposed to a human brain-like environment adapt by altering their
308 gene expression profiles towards increased glycolysis, reduced proliferation, and
309 increased invasiveness and angiogenesis, all of which are hallmarks of GBM within their
310 native state *in vivo*.
311
312 **Neural cells in organoids-GBM-chimeras undergo transcriptional changes**
313 **consistent with altered oxidative stress, angiogenesis, and neurodifferentiation.**
314 Our understanding of the effects of tumor cells on normal brain development is
315 limited due to the inaccessibility of normal human brain tissue. We reasoned that
316 comparing cell compositions and gene expression profiles of organoids and organoids in
317 chimeras could provide unique insights into the effects of tumor cells on normal human
318 brain development. To compare and contrast the properties of neural cells in chimeras
319 and organoids, we co-clustered RFP-expressing organoid cells from chimeras (MS-GBM
320 chimeras: 1,188 cells and PN-GBM chimeras: 2,295 cells) with those from H9 and iPSC-
321 derived RFP-expressing organoids (17,893 cells) (**Fig. 5A-B** and **Supplementary**

322 **Dataset 7**). This analysis revealed that the compositions of neural cell clusters and the
323 proportions of cells in different clusters remained relatively similar between organoids and
324 chimeras (**Fig. 5C-E**). The identified cell clusters could be broadly divided into the clusters
325 of NPs (clusters: 4, 9, 10, and 11) and GABAergic neurons (clusters: 0, 1, 2, 3, 5, 6, 8,
326 and 12) (**Fig. 5F**). To identify differentially expressed genes and molecular pathways
327 between NPs and GABAergic neurons in organoids and chimeras, we performed a
328 'pseudo-bulks' mRNA-seq analysis (Squair et al. 2021) on the combined clusters of NPs
329 and neurons (**Fig. 5F**). Both NPs and neurons in chimeras were different from those in
330 organoids; however, the dissimilarity between the neurons in chimeras was significantly
331 greater than that of the NPs (**Fig. 5G-H**). To identify dysregulated neuronal pathways, we
332 performed GSEA analysis on DEGs identified in neurons (**Fig. 5I** and **Supplementary**
333 **Dataset 8**) and NPs (**Fig. 5J** and **Supplementary Dataset 9**). The molecular pathways
334 "*response decreased oxygen levels"* and *"response to hypoxia"* were upregulated in both
335 neurons and NPs from chimeras as compared to those from organoids (**Fig. 5I-J**). This
336 finding suggests that GBMs induce the formation of a hypoxic pro-tumorigenic
337 environment in organoids. The hypoxic microenvironment has been associated with
338 aggressive and therapy-resistant tumors (Ye et al. 2022) and with the abnormal
339 specification of human cortical neurons (Bhaduri, Andrews, et al. 2020). In addition, we
340 observed increased enriched molecular pathways "*positive regulation of vasculature*
341 *development" and "angiogenesis"* in neurons, and upregulation of pro-angiogenesis gene
342 *VEGFA* in NPs (**Fig. 5I-J**), suggesting that GBMs promote the formation of a pro-
343 angiogenic hypoxic microenvironment in neural tissue by altering the gene expression
344 profiles of neural cells.

345 In neurons from chimeras, the down-regulated molecular pathways were "*synapse*
346 *assembly*", "*synapse organization",* and "*ion channel activity*" (**Fig. 5l**), suggesting
347 potential impairments of neuronal differentiation and maturation of neurons in chimeras
348 by tumor cells. This is consistent with a previous study that reported decreased inhibitory
349 synapses in a patient-derived xenograft mouse model (Yu et al. 2020). Together, these
350 results show that normal neural development is impacted by GBM tumors, which cause
351 impaired neuronal differentiation and maturation and increased formation of a pro-
352 tumorigenic environment, similar to what was previously observed in patients and
353 xenotransplantation models (Osswald et al. 2015; Venkataramani et al. 2019, 2022;
354 Hausmann et al. 2022).
355

356 **DISCUSSION**

357 In this study, we fused patient-derived PN- and MS-GBMs with human subpallial
358 telencephalic organoids to investigate the effects of the human brain-like environment on
359 tumor cells and the effects of GBM tumors on human brain development. We observed
360 efficient propagation of GBM tumors in chimeras without the need for exogenous growth
361 factors and substantial changes in gene expression profiles in both tumor and neural
362 cells. Collectively, our findings suggest that tumor and normal neural cells extensively
363 interact with each other in organoid-GBM chimeras and that the use of organoid-GBM
364 chimeras may provide a physiologically relevant microenvironment for propagating GBM
365 cells in vitro for future mechanistic insights and therapy development.
366

367 The fusion of GBMs with human stem-derived organoids has been investigated in
368 several previous studies (Bian et al. 2018b; da Silva et al. 2018b; Ogawa et al. 2018b;
369 Linkous et al. 2019b; Pine et al. 2020b). These studies demonstrated that GBM cells can
370 spontaneously penetrate the organoids and form interconnected networks of tumor and
371 "normal" cells. Similar to the previous studies, we also observed an efficient fusion of
372 GBMs with human stem cell-derived organoids. In contrast to those studies, we fused
373 GBMs with well-defined (in terms of cellular composition) subpallial telencephalic
374 organoids. Both PN- and MS-GBMs demonstrated an elevated expression of the
375 subpallial telencephalic marker genes, suggesting that subpallial NPCs may give rise to
376 GBM tumors (Sanai et al. 2005; Eichmüller et al. 2022) and provide a more supportive
377 microenvironment for growing GBM tumors *in vitro*.
378
379 Unlike in GBM spheroids, we observed that tumor cells in organoid-GBM chimeras
380 efficiently propagated without supplementation of exogenous EGF and FGF. EGF and
381 FGF are commonly used for propagating GBM spheroids *in vitro* (Lee et al. 2006b). These
382 factors promote tumor cell survival and proliferation by activating the MAPK/ERK and
383 PI3K/AKT/mTOR signaling pathways (Schlessinger 2000). However, the physiological
384 concentration of these factors in the brain is largely unknown and may vary depending on
385 the brain region, microenvironmental niche, age, physiological state, or pathological state.
386 We found that GBM tumors showed limited propagation in spheroids without exogenous
387 EGF and FGF but robust propagation in chimeras. These results suggest that either
388 normal neural cells in organoids provide GBMs with EGF and FGF or alternative signaling
389 cascades are activated in tumor cells for survival and propagation without these growth

390 factors. As we also found no The specific signaling cascades activated in tumor cells by
391 organoids remain to be understood.
392
393 Differentially expressed genes detected in GBM tumors in chimeras compared to those
394 in spheroids (**Fig. 4**) may provide insights into the molecular programs involved in
395 promoting tumor cell survival and propagation in chimeras. Among the upregulated genes
396 in chimeras, we found transcription factor *ATF3*, associated with stress responses and
397 more aggressive tumor behavior with poor prognosis (Xu et al. 2022); mitophagy
398 regulators *BNIP3* and *BNIP3L* (Ney 2015), activated with hypoxia (Jung et al. 2019),
399 which is a common feature of the tumor microenvironment (Zhou et al. 2011); and the
400 MAPK/ERK pathway genes *FOS*, *DDIT3*, and *VEGFA* (Bao et al. 2006; Venkatesh et al.
401 2015), which are known to promote tumor cells survival and propagation. This suggests
402 that oxidative stress induced by hypoxia and the MAPK/ERK pathway may be involved in
403 supporting tumor cells in organoid-GBM chimeras.
404
405 Interestingly, we also found that GBM tumors in chimeras showed dramatically
406 reduced expression of multiple genes associated with cell cycle proliferation (**Fig. 4**).
407 Reduced proliferation is a hallmark of quiescent stem cells (Hanahan 2022). The
408 quiescent tumor stem cells are characterized by slow rates of division (Antonica et al.
409 2022) and, thus, are difficult to target with irradiation or chemotherapies (Xie et al. 2022).
410 Interestingly, it was demonstrated that GBM cells in organoid-GBM chimeras are
411 substantially more resistant to irradiation (Linkous et al. 2019b). Our results suggest that
412 the reduced proliferation of GBM tumors in chimeras is potentially responsible for this

413 radioresistance. Interestingly, we found no increase in the expression levels of multiple
414 quiescence genes in chimeras. Instead, different sets of quiescence genes were
415 upregulated in different GBM tumors under different experimental conditions (**Fig. 4N**).
416 These results suggest that the tumor-specific microenvironment may be involved in
417 defining the tumor-specific quiescence signature and that alternative culture conditions
418 such as organoid-GBM chimeras could be useful for studying the pathology of GBMs in
419 the brain.
420
421 Another interesting observation of this study was that the co-culture of PN-GBM with
422 subpallial telencephalic organoids that consist of GABAergic NPCs and neurons induced
423 gene expression changes in PM-GBM consistent with the acquisition of mesenchymal
424 cell identity (Bhat et al. 2013). PN to MS transition (PMT) in GBM has been previously
425 observed in response to NF-kB exposure (Bhat et al. 2013), serum exposure
426 (Balasubramaniyan et al. 2015), TGFβ exposure (Joseph et al. 2014), activation of the
427 Notch signaling pathway (Cheng et al. 2017), and mutations in tumor suppressor genes
428 such as PTEN and P53 (Behnan et al. 2019). In addition, changes in the tumor
429 microenvironment, including hypoxia and inflammation, have been reported to promote
430 the PMT microenvironment (Tejero et al. 2019). PMT is associated with increased tumor
431 cell motility, invasiveness, and therapy resistance (Bhat et al. 2013). Our results support
432 the idea that the environment in organoid-GBM chimeras promotes PMT. However,
433 additional functional experiments are required to confirm the mesenchymal-like identities
434 of PN-GBM tumors in chimeras.
435

436 Finally, in this study, we also investigated the effects of tumor cells on gene
437 expression profiles of neural cells in organoids. The detected gene expression changes
438 are consistent with impaired neural development and functional maturation, as well as
439 increased angiogenesis and response to hypoxia (**Fig. 5**). Interestingly, a recent study
440 showed that cell stress impairs the specification of oRG cells and neurons in organoids
441 (Bhaduri, Andrews, et al. 2020), suggesting that the hypoxic stress affects the normal
442 development in organoid-GBM chimeras. Moreover, the effect of GBMs on GABAergic
443 neurons in organoid-GBM chimeras may lead to impaired function and elevated
444 excitability due to the disinhibition of excitatory neurons and neural networks. Indeed,
445 elevated excitability was observed in a recent study where authors demonstrated that
446 GBM cells express high levels of IGSF3, an interactor of the potassium channel Kir4.1
447 that suppresses potassium buffering leading to spreading depolarization (Curry et al.
448 2023). Finally, another recent study showed increased hyperexcitability, increased
449 PSD95^{+} excitatory synapses, and decreased Gephyrin^{+} inhibitory synapses in the
450 peritumoral regions of mice transplanted with patient-derived GBM cells (Yu et al. 2020).
451 Together, these results support the idea that GBM cells have a profound effect in
452 remodeling the peritumoral neuronal network towards a state of hyperexcitability, with a
453 selective detrimental effect on inhibitory synapses.
454
455 In summary, we demonstrated an efficient propagation of GBM tumors *in vitro* by
456 fusing them with subpallial telencephalic organoids in chimeras. We also found that GBM
457 cells adapt to the developing human brain microenvironment by altering gene expressions
458 associated with the PN to MS transition, proliferation, hypoxia, and angiogenesis. In

459 addition, the presence of GBM cells impacted the properties of neural cells in the
460 organoids that were consistent with impaired neuronal differentiation and increased
461 angiogenesis. Collectively, this study provides important insights into the molecular
462 pathways that could be targeted for therapy development. Future work will be needed to
463 explore cell-cell communications between organoids and GBM tumor cells to elucidate
464 the underlying cellular and molecular mechanisms. Finally, future studies should also
465 investigate the contributions of different types of NPCs, inhibitory and excitatory neurons,
466 and different types of glial cells on GBM tumor survival, propagation, and treatment
467 resistance.
468
469
470
471
472
473
474
475
476
477
478
479
480
481

482 **MATERIALS AND METHODS**

483 **Cell lines**

484 The GBM cell lines used in this study are: GBM11 (PN), GBM established cell line (Bhat
485 et al., 2013) and GBM20 (MS), GBM established cell line (Bhat *et al.*, 2013). The hPSC
486 lines used in this study are: mTagRFP-T hiPSCs (Allen Cell Collection, Cat # AICS-0054-
487 091) and H9 hESCs (WiCell). Both hPSC lines were obtained from healthy donors.

488

489 **Generating Single Neural Rosette-derived Organoids**

490 The iPSCs were grown in the StemFlex/E8 medium (1:1 mixture of StemFlex
491 (ThermoFisher, Cat # A3349401) and E8 (ThermoFisher, Cat # A3349401) media).
492 The iPSCs were differentiated in the N2/B27 medium containing a 1:1 mixture of
493 DMEM/F12 and Neurobasal-A, 1X N2 supplement (ThermoFisher Scientific), 1X B27
494 supplement with vitamin A (ThermoFisher Scientific), 2 µg/ml of Heparin, 1X GlutaMAX
495 (ThermoFisher Scientific), and 1X MEM-NEAA. The N2/B27 medium was supplemented
496 with 4 µM Dorsomorphin (Tocris, Cat # 3039) and 10 µM SB431542 (Tocris, Cat # 1614).
497 SNR-derived organoids were generated as previously described (Wang et al., 2022).
498 Briefly, the differentiated iPSCs were grown to rosettes in N2/B27 medium for 6 days.
499 Single neural rosettes were picked and grown to single neural rosette-derived organoids
500 in N2/B27 medium with 10 ng/ml of each EGF and FGF for 1-3 days without agitation and
501 then with agitation for 2-3 weeks.

502

503 **Growing GBM Spheres**

504 GBM11 and GBM20 spheres were growing as described previously (Bhat *et al.*, 2013).
505 Briefly, GBM cells were incubated in a nontreated tissue culture flask in the GBM spheres
506 medium containing DMEM/F12 Medium, 2X B-27 supplement (Life Technologies, Cat #
507 17504-044), 1X Normocin (InvivoGen, Cat # ant-nr-1), 20 ng/ml EGF (Life Technologies,
508 Cat # PHG0311) and 20 ng/ml FGF (Life Technologies, Cat # 13256-029). To maintain
509 the proliferation, spheres must be triturated to single cells/small clumps once visible
510 spheres appear.
511

512 **Generating Organoid-GBM Chimeras**

513 To generate organoid-GBM chimeras, 2-3 week-old SNR-organoids were individually
514 transferred to a V-shaped non-treated 96-well plate containing N2/B27 medium (no
515 EGF/FGF), one organoid per well. 2-4 GBM spheres were added to each organoid/well.
516 Organoid-GBM chimeras were incubated in a 37ºC/5% CO_2 incubator for 12-14 days with
517 media change every other day. Organoid-GBM chimeras were then transferred to 24-well
518 non-treated plates and maintained in a 37ºC/5% CO_2 incubator with agitation (~45rpm)
519 on an orbital shaker for one week. The media were changed every other day.
520

521 **Immunohistochemistry and confocal imaging**

522 1 month old single neural rosettes (SNR)-derived organoids were fixed in 4%
523 paraformaldehyde overnight at 4°C and washed with PBS and the organoids were then
524 passed through a sequential sucrose solution gradient of 10%, 20% and 30%
525 respectively. Organoids were placed in cryosectioning molds, embedded in OCT and
526 flash frozen and stored at -80°C. Then organoids were cut at 15-20 μm thickness using a

527 Leica Cryostat machine and adhered to positively charged microscope slides.
528 Cryosections were then processed for immunostaining as follows: Sections were washed
529 with 0.1M glycine in PBS and then blocked with 0.3% Triton-X 100 with 3% Bovine cerium
530 albumin (BSA) in PBS for 1-2 h at room temperature. Primary antibodies were diluted in
531 0.3% Triton-X 100 with 3% BSA in PBS and left overnight at cold room. The following
532 primary antibodies were used: mouse anti-PAX6 (DSHB, 1:50), sheep anti-TBR2 (R&D
533 Systems, AF6166, 1:200), mouse anti-MASH1 (Invitrogen, 1:200), rat anti-CTIP2
534 (Abcam, ab18465, 1:200), rabbit anti-GSX2 (Invitrogen, PA5-35887, 1:200), mouse anti
535 GAD67 (Millipore, MAB5406, 1: 200), mouse anti-SOX2 (Santa cruz, sc-365823, 1:200),
536 rabbit anti-RFP (Evrogen, AB234, 1:1000), chicken anti-GFP (Novus, NB100-1614,
537 1:500). The next day, sections were washed with PBS for 15 min and secondary
538 antibodies were also diluted with 0.3% Triton-X 100 with 3% BSA in PBS. The secondary
539 antibodies coupled to Alexa Fluor fluorescent dyes (Invitrogen) were added 1:1000 ration
540 in combination with DAPI (1:1000) for 1-2 h at room temperature in the dark. After 15 min
541 PBS washes, slides were mounted with coverslips using Aqua Poly Mounting Media, left
542 to dry at room temperature in the dark and stored at -20°C for imaging. Fluorescent
543 imaging was performed using Zeiss 880 Airyscan confocal microscopes using 10x and
544 20x objective at the University of Utah Cell Imaging Core Facility and data processing
545 and quantification was performed using Fiji, and/or CellProfiler software.
546

547 **Tissue clearing and confocal imaging**

548 Organoids-GBM chimeras were fixed with fresh 4% paraformaldehyde (PFA) (Cat#
549 15710) for 24 hours at 4°C. The fixed organoids were then cleared following a modified

550 SWITCH protocol developed by the Chung Lab (Murray et al. 2015). Briefly, chimeras
551 were transferred to a fixation-OFF solution and incubated at 4°C for 1 day. Subsequently,
552 chimeras were transferred to fixation-ON solution and incubated for 1 day at 4°C. To
553 inactivate the fixative solution, chimeras were washed twice with PBST at room
554 temperature for 1 hour each and then submerged into fixative-inactivation solution at 37°C
555 overnight. Subsequently, chimeras were washed twice with thermal clearing solution for
556 1 hour each at 37°C. To achieve complete lipid clearing, chimeras were immersed in fresh
557 thermal clearing solution and incubated overnight at 37°C. Finally, to achieve maximal
558 optical clearing, chimeras were placed in 500 µL refracting index matching solution
559 (RIMS) at 37°C for 1 hour. All incubations and wash volumes used were 10 mL, incubation
560 conditions were stationary and in the dark to preserve chromophores. For imaging,
561 chimeras were mounted on a glass slide using 1 mm thick homemade silicone ring
562 spacer, filled with RIMS, and covered with a glass cover slip to avoid drying up and air
563 bubbles. Fluorescent imaging was performed at the University of Utah Cell Imaging Core
564 Facility using a Zeiss LSM 880 Airyscan confocal microscope equipped with a Plan-
565 Neofluar 10X/0.30 M27 objective, 488 nm and 568 nm laser to acquire high-resolution
566 images. We used a refractive index of 1.46 and a total of 64 Z-stacks were acquired to
567 cover the entire thickness of the sample. To create 3D reconstructions and a video, we
568 used Imaris Cell Imaging (Bitplane) and Fiji softwares.
569

570 **Single-cell collection from organoids and GBM-organoids chimeras**

571 SNR-derived organoids were rinsed with sterile Dulbecco's phosphate-buffered saline
572 (DPBS, 1X) and chopped in small pieces using a scalpel. Organoids' pieces were

573 collected in 1.5 mL tubes in DPBS and centrifuged for 2 minutes at 1000 rpm. Samples
574 were incubated in pre-warmed papain (Worthington Biochemical) containing 5% DNaseI
575 (Sigma) at 37°C for 50 minutes. After incubation, cells were resuspended in Trypsin
576 Inhibitor (Sigma) and manually triturated by pipetting up and down using P1000 pipette.
577 Cells were centrifuged for 5 minutes at 1000 rpm before the next step. Cells were
578 resuspended in cold DPBS containing 0.04% BSA. Samples were kept on ice from this
579 point forward. Samples were quickly transferred to the High Throughput Genomics Core
580 Facility at the University of Utah for cell viability assessment.
581

582 **Library preparation and raw data processing for single-cell RNA-seq**

583 Single-cell capture, lysis, and cDNA synthesis were performed with the 10x Genomics
584 Chromium at the High Throughput Genomics Core Facility at the University of Utah.
585 Single cells were loaded onto 10x Genomics Single Cell 3' Chips along with the master
586 mix following the manufacturer's instruction for the Chromium Single Cell 3′ Library (v3.1).
587 The resulting libraries were sequenced on an Illumina NovaSeq 6000 in a 150 × 150 cycle
588 paired-end sequencing mode using a NovaSeq 6000 S4 reagent Kit v1.5. Pre-processing
589 of reads was conducted using the Cell Ranger pipeline (10x Genomics) with alignment to
590 GRCh37 (hg19) reference assembly built with the addition of GFP and RFP sequences.
591 Gene-barcoded matrices were constructed for each sample by counting unique molecular
592 identifiers (UMIs). The single-cell RNA-seq data reported in this paper is available in the
593 GEO repository with the following accession number (to be provided).
594

595 **Clustering analysis and removal of stressed cells in organoids**

596 Downstream analysis of single-cell RNA-seq matrix files was conducted using Seurat (v
597 4.2.0 and R version 4.1.2). Cells were selected and filtered out based on QC metrics
598 distributions across samples of the same experimental condition (number of unique genes
599 detected in each cell [cells with less than 200 genes detected were filtered out], total
600 number of molecules detected in each cell, and percentage of reads that map to the
601 mitochondrial genome). Single cell expression values were normalized, and the top 2000
602 highly variable genes were identified using *FindVariableFeatures* function. Data were
603 then scaled, and principal component analysis (PCA) was performed using 50
604 dimensions. Data integration between different samples was performed with Harmony
605 algorithm. The *ElbowPlot* function was then used to pick the relevant dimensions. The top
606 10 principal components were used for running UMAP dimensional reduction technique
607 and for clustering using Seurat's *FindNeighbors* and *FindCluster* functions (original
608 Louvain algorithm, resolution 1.0). Cluster identities were assigned based on (I) cluster
609 gene markers as determined by *FindAllMarkers* function, (II) gene expression values of
610 known telencephalic or GBM markers, and (III) cluster correlation as determined by
611 *clustify* function (Spearman ranked correlation, clustifyr package v 1.6.0). Identification of
612 stressed cells in organoids was performed using the package *gruffi* (v. 0.7.2) using default
613 parameters and without adjusting manually the thresholds estimated by *gruffi*. Stressed
614 cells were removed from the dataset before further analysis.
615

616 **Differential expression analysis**

617 Differential gene expression analysis between clusters in different samples was
618 performed using the *FindMarkers* function (Wilcoxon rank sum test) and genes with an

619 adjusted (Bonferroni's correction) p-value < 0.05 were considered significant. Volcano
620 plots of significant differentially expressed genes were generated using the
621 *EnhancedVolcano* function (|FoldChange| > 0.5 and adjusted pvalue < 0.05) from the
622 EnhancedVolcano package (v. 1.12.0). Differential gene expression analysis between
623 different samples was performed calculating pseudo bulk values using first the
624 *SingleCellExperiment* function (SingleCellExperiment package, v. 1.16.0) to convert
625 Seurat objects and then the *aggregate.Matrix* function (fun = "sum", package Matrix.utils
626 v. 0.9.8) to generate pseudo bulk RNA-seq datasets. Pseudo bulk datasets were passed
627 to the *DESeq* function (DESeq2 package, v. 1.34.0) to calculate differentially expressed
628 genes.
629
630 **Cell state scoring**
631 Cell state scores were calculated using the lists of gene signatures (NPC-like, OPC-like,
632 AC-like, and MES-like) previously reported in Neftel et al. 2019. For each tumor cell a
633 signature score value was calculated using the *AddModuleScore_UCell* function from the
634 UCell package (v.). The NPC, OPC, AC or MES identity was assigned to each cell by
635 looking at the maximum signature score value. The pie charts with the percentages of
636 each cell state per GBM type were generated using the *pie* function.
637
638 **Gene Set Enrichment Analysis**
639 Gene Set Enrichment Analysis was performed using the *gseGO* function from the
640 clusterProfiler package (v. 4.2.2). Gene-concept networks were generated using the
641 *cnetplot* function from the enrichplot package (v. 1.14.2).

734 **REFERENCES:**

735 Antonica F, Santomaso L, Pernici D, Petrucci L, Aiello G, Cutarelli A, Conti L, Romanel A,
736 Miele E, Tebaldi T, Tiberi L. 2022. A slow-cycling/quiescent cells subpopulation is involved
737 in glioma invasiveness. Nat Commun. 13.

738 Balasubramaniyan V, Vaillant B, Wang S, Gumin J, Butalid ME, Sai K, Mukheef F, Kim H,
739 Boddeke HWGM, Lang F, Aldape K, Sulman EP, Bhat KP, Colman H. 2015. Aberrant
740 mesenchymal differentiation of glioma stem-like cells: implications for therapeutic targeting.

741 Bao S, Wu Q, Sathornsumetee S, Hao Y, Li Z, Hjelmeland AB, Shi Q, McLendon RE,
742 Bigner DD, Rich JN. 2006. Stem cell-like glioma cells promote tumor angiogenesis through
743 vascular endothelial growth factor. Cancer Res. 66:7843–7848.

744 Behnan J, Finocchiaro G, Hanna G. 2019. The landscape of the mesenchymal signature in
745 brain tumours. Brain.

746 Berezovsky AD, Poisson LM, Cherba D, Webb CP, Transou AD, Lemke NW, Hong X,
747 Hasselbach LA, Irtenkauf SM, Mikkelsen T, de Carvalho AC. 2014. Sox2 promotes
748 malignancy in glioblastoma by regulating plasticity and astrocytic differentiation. Neoplasia
749 (United States). 16:193-206.e25.

750 Bershteyn M, Nowakowski TJ, Pollen AA, Di Lullo E, Nene A, Wynshaw-Boris A, Kriegstein
751 AR. 2017. Human iPSC-Derived Cerebral Organoids Model Cellular Features of
752 Lissencephaly and Reveal Prolonged Mitosis of Outer Radial Glia. Cell Stem Cell. 20:435-
753 449.e4.

754 Bhaduri A, Andrews MG, Mancia Leon W, Jung D, Shin D, Allen D, Jung D, Schmunk G,
755 Haeussler M, Salma J, Pollen AA, Nowakowski TJ, Kriegstein AR. 2020. Cell stress in
756 cortical organoids impairs molecular subtype specification. Nature. 578:142–148.

757 Bhaduri A, di Lullo E, Jung D, Müller S, Crouch EE, Espinosa CS, Ozawa T, Alvarado B,
758 Spatazza J, Cadwell CR, Wilkins G, Velmeshev D, Liu SJ, Malatesta M, Andrews MG,
759 Mostajo-Radji MA, Huang EJ, Nowakowski TJ, Lim DA, Diaz A, Raleigh DR, Kriegstein AR.
760 2020. Outer Radial Glia-like Cancer Stem Cells Contribute to Heterogeneity of
761 Glioblastoma. Cell Stem Cell. 26:48-63.e6.

762 Bhat KPL, Balasubramaniyan V, Vaillant B, Ezhilarasan R, Hummelink K, Hollingsworth F,
763 Wani K, Heathcock L, James JD, Goodman LD, Conroy S, Long L, Lelic N, Wang S,
764 Gumin J, Raj D, Kodama Y, Raghunathan A, Olar A, Joshi K, Pelloski CE, Heimberger A,
765 Kim SH, Cahill DP, Rao G, DenDunnen WFA, Boddeke HWGM, Phillips HS, Nakano I,
766 Lang FF, Colman H, Sulman EP, Aldape K. 2013. Mesenchymal Differentiation Mediated
767 by NF-κB Promotes Radiation Resistance in Glioblastoma. Cancer Cell. 24:331–346.

768 Bian S, Repic M, Guo Z, Kavirayani A, Burkard T, Bagley JA, Krauditsch C, Knoblich JA.
769 2018a. Genetically engineered cerebral organoids model brain tumor formation. Nat
770 Methods. 15:631–639.

771 Bian S, Repic M, Guo Z, Kavirayani A, Burkard T, Bagley JA, Krauditsch C, Knoblich JA.
772 2018b. Genetically engineered cerebral organoids model brain tumor formation. Nat
773 Methods. 15:631–639.

774 Brat DJ, Aldape K, Colman H, Holland EC, Louis DN, Jenkins RB, Kleinschmidt-DeMasters
775 BK, Perry A, Reifenberger G, Stupp R, von Deimling A, Weller M. 2018. cIMPACT-NOW
776 update 3: recommended diagnostic criteria for “Diffuse astrocytic glioma, IDH-wildtype, with
777 molecular features of glioblastoma, WHO grade IV”. Acta Neuropathol. 136:805–810.

Cheng W, Zhang C, Ren X, Jiang Y, Han S, Liu Y, Cai J, Li M, Wang K, Liu Y, Hu H, Li Q, Yang P, Bao Z, Wu A. 2017. Bioinformatic analyses reveal a distinct Notch activation induced by STAT3 phosphorylation in the mesenchymal subtype of glioblastoma. J Neurosurg. 126:249–259.

Colman H, Zhang L, Sulman EP, McDonald JM, Shooshtari NL, Rivera A, Popoff S, Nutt CL, Louis DN, Cairncross JG, Gilbert MR, Phillips HS, Mehta MP, Chakravarti A, Pelloski CE, Bhat K, Feuerstein BG, Jenkins RB, Aldape K. 2010. A multigene predictor of outcome in glioblastoma. Neuro Oncol. 12:49–57.

Couturier CP, Ayyadhury S, Le PU, Nadaf J, Monlong J, Riva G, Allache R, Baig S, Yan X, Bourgey M, Lee C, Wang YCD, Wee Yong V, Guiot MC, Najafabadi H, Misic B, Antel J, Bourque G, Ragoussis J, Petrecca K. 2020a. Single-cell RNA-seq reveals that glioblastoma recapitulates a normal neurodevelopmental hierarchy. Nat Commun. 11.

Couturier CP, Ayyadhury S, Le PU, Nadaf J, Monlong J, Riva G, Allache R, Baig S, Yan X, Bourgey M, Lee C, Wang YCD, Wee Yong V, Guiot MC, Najafabadi H, Misic B, Antel J, Bourque G, Ragoussis J, Petrecca K. 2020b. Single-cell RNA-seq reveals that glioblastoma recapitulates a normal neurodevelopmental hierarchy. Nat Commun. 11.

Curry RN, Aiba I, Meyer J, Lozzi B, Ko Y, McDonald MF, Rosenbaum A, Cervantes A, Huang-Hobbs E, Cocito C, Greenfield JP, Jalali A, Gavvala J, Mohila C, Serin Harmanci A, Noebels J, Rao G, Deneen B. 2023. Glioma epileptiform activity and progression are driven by IGSF3-mediated potassium dysregulation. Neuron.

da Silva B, Mathew RK, Polson ES, Williams J, Wurdak H. 2018a. Spontaneous Glioblastoma Spheroid Infiltration of Early-Stage Cerebral Organoids Models Brain Tumor Invasion. SLAS Discovery. 23:862–868.

da Silva B, Mathew RK, Polson ES, Williams J, Wurdak H. 2018b. Spontaneous Glioblastoma Spheroid Infiltration of Early-Stage Cerebral Organoids Models Brain Tumor Invasion. SLAS Discovery. 23:862–868.

Eichmüller OL, Corsini NS, Vértesy Á, Morassut I, Scholl T, Gruber VE, Peer AM, Chu J, Novatchkova M, Hainfellner JA, Paredes MF, Feucht M, Knoblich JA. 2022. Amplification of human interneuron progenitors promotes brain tumors and neurological defects. Science (1979). 375.

Eiraku M, Watanabe K, Matsuo-Takasaki M, Kawada M, Yonemura S, Matsumura M, Wataya T, Nishiyama A, Muguruma K, Sasai Y. 2008. Self-Organized Formation of Polarized Cortical Tissues from ESCs and Its Active Manipulation by Extrinsic Signals. Cell Stem Cell.

Hanahan D. 2022. Hallmarks of Cancer: New Dimensions. Cancer Discov. 12:31–46.

Hausmann D, Hoffmann DC, Venkataramani V, Jung E, Horschitz S, Tetzlaff SK, Jabali A, Hai L, Kessler T, Azoŕin DD, Weil S, Kourtesakis A, Sievers P, Habel A, Breckwoldt MO, Karreman MA, Ratliff M, Messmer JM, Yang Y, Reyhan E, Wendler S, Löb C, Mayer C, Figarella K, Osswald M, Solecki G, Sahm F, Garaschuk O, Kuner T, Koch P, Schlesner M, Wick W, Winkler F. 2022. Autonomous rhythmic activity in glioma networks drives brain tumour growth. Nature.

Hu LS, Ning S, Eschbacher JM, Baxter LC, Gaw N, Ranjbar S, Plasencia J, Dueck AC, Peng S, Smith KA, Nakaji P, Karis JP, Quarles CC, Wu T, Loftus JC, Jenkins RB, Sicotte H, Kollmeyer TM, O'Neill BP, Elmquist W, Hoxworth JM, Frakes D, Sarkaria J, Swanson KR, Tran NL, Li J, Mitchell JR. 2017. Radiogenomics to characterize regional genetic heterogeneity in glioblastoma. Neuro Oncol. 19:128–137.

824 Huse JT, Phillips HS, Brennan CW. 2011. Molecular subclassification of diffuse gliomas:
825 seeing order in the chaos. Glia. 59:1190–1199.

826 Jacob F, Salinas RD, Zhang DY, Nguyen PTT, Schnoll JG, Wong SZH, Thokala R, Sheikh
827 S, Saxena D, Prokop S, Liu D ao, Qian X, Petrov D, Lucas T, Chen HI, Dorsey JF,
828 Christian KM, Binder ZA, Nasrallah M, Brem S, O'Rourke DM, Ming G li, Song H. 2020. A
829 Patient-Derived Glioblastoma Organoid Model and Biobank Recapitulates Inter- and Intra-
830 tumoral Heterogeneity. Cell. 180:188-204.e22.

831 Joseph J V., Conroy S, Tomar T, Eggens-Meijer E, Bhat K, Copray S, Walenkamp AME,
832 Boddeke E, Balasubramanyian V, Wagemakers M, Den Dunnen WFA, Kruyt FAE. 2014.
833 TGF-β is an inducer of ZEB1-dependent mesenchymal transdifferentiation in glioblastoma
834 that is associated with tumor invasion. Cell Death Dis. 5.

835 Jung E, Osswald M, Ratliff M, Dogan H, Xie R, Weil S, Hoffmann DC, Kurz FT, Kessler T,
836 Heiland S, von Deimling A, Sahm F, Wick W, Winkler F. 2021. Tumor cell plasticity,
837 heterogeneity, and resistance in crucial microenvironmental niches in glioma. Nat
838 Commun. 12.

839 Jung J, Zhang Y, Celiku O, Zhang W, Song H, Williams BJ, Giles AJ, Rich JN, Abounader
840 R, Gilbert MR, Park DM. 2019. Mitochondrial Nix promotes tumor survival in the hypoxic
841 niche of glioblastoma. Cancer Res. 79:5218–5232.

842 Kadoshimaa T, Sakaguchi H, Nakanoa T, Soena M, Ando S, Eirakuc M, Sasai Y. 2013.
843 Self-organization of axial polarity, inside-out layer pattern, and species-specific progenitor
844 dynamics in human ES cell-derived neocortex. Proceedings of the National Academy of
845 Sciences. 110:20285–20289.

846 Lancaster MA, Renner M, Martin CA, Wenzel D, Bicknell LS, Hurles ME, Homfray T,
847 Penninger JM, Jackson AP, Knoblich JA. 2013. Cerebral organoids model human brain
848 development and microcephaly. Nature.

849 Lauko A, Lo A, Ahluwalia MS, Lathia JD. 2022. Cancer cell heterogeneity & plasticity in
850 glioblastoma and brain tumors. Semin Cancer Biol.

851 Le Rhun E, Preusser M, Roth P, Reardon DA, van den Bent M, Wen P, Reifenberger G,
852 Weller M. 2019. Molecular targeted therapy of glioblastoma. Cancer Treat Rev.

853 Ledur PF, Onzi GR, Zong H, Lenz G. 2017. Culture conditions defining glioblastoma cells
854 behavior: what is the impact for novel discoveries? Oncotarget. 8:69185–69197.

855 Lee J, Kotliarova S, Kotliarov Y, Li A, Su Q, Donin NM, Pastorino S, Purow BW,
856 Christopher N, Zhang W, Park JK, Fine HA. 2006a. Tumor stem cells derived from
857 glioblastomas cultured in bFGF and EGF more closely mirror the phenotype and genotype
858 of primary tumors than do serum-cultured cell lines. Cancer Cell. 9:391–403.

859 Lee J, Kotliarova S, Kotliarov Y, Li A, Su Q, Donin NM, Pastorino S, Purow BW,
860 Christopher N, Zhang W, Park JK, Fine HA. 2006b. Tumor stem cells derived from
861 glioblastomas cultured in bFGF and EGF more closely mirror the phenotype and genotype
862 of primary tumors than do serum-cultured cell lines. Cancer Cell. 9:391–403.

863 Lee J, Son MJ, Woolard K, Donin NM, Li A, Cheng CH, Kotliarova S, Kotliarov Y, Walling J,
864 Ahn S, Kim M, Totonchy M, Cusack T, Ene C, Ma H, Su Q, Zenklusen JC, Zhang W, Maric
865 D, Fine HA. 2008. Epigenetic-Mediated Dysfunction of the Bone Morphogenetic Protein
866 Pathway Inhibits Differentiation of Glioblastoma-Initiating Cells. Cancer Cell. 13:69–80.

867 Linkous A, Balamatsias D, Snuderl M, Edwards L, Miyaguchi K, Milner T, Reich B, Cohen-
868 Gould L, Storaska A, Nakayama Y, Schenkein E, Singhania R, Cirigliano S, Magdeldin T,

869 Lin Y, Nanjangud G, Chadalavada K, Pisapia D, Liston C, Fine HA. 2019a. Modeling
870 Patient-Derived Glioblastoma with Cerebral Organoids. Cell Rep. 26:3203-3211.e5.

871 Linkous A, Balamatsias D, Snuderl M, Edwards L, Miyaguchi K, Milner T, Reich B, Cohen-
872 Gould L, Storaska A, Nakayama Y, Schenkein E, Singhania R, Cirigliano S, Magdeldin T,
873 Lin Y, Nanjangud G, Chadalavada K, Pisapia D, Liston C, Fine HA. 2019b. Modeling
874 Patient-Derived Glioblastoma with Cerebral Organoids. Cell Rep. 26:3203-3211.e5.

875 Louis DN, Perry A, Wesseling P, Brat DJ, Cree IA, Figarella-Branger D, Hawkins C, Ng HK,
876 Pfister SM, Reifenberger G, Soffietti R, Von Deimling A, Ellison DW. 2021. The 2021 WHO
877 classification of tumors of the central nervous system: A summary. Neuro Oncol. 23:1231–
878 1251.

879 Lui JH, Hansen D v., Kriegstein AR. 2011. Development and evolution of the human
880 neocortex. Cell.

881 Mariani J, Simonini MV, Palejev D, Tomasini L, Coppola G, Szekely AM, Horvath TL,
882 Vaccarino FM. 2012. Modeling human cortical development in vitro using induced
883 pluripotent stem cells. Proceedings of the National Academy of Sciences. 109:12770–
884 12775.

885 Monje M, Borniger JC, D'Silva NJ, Deneen B, Dirks PB, Fattahi F, Frenette PS, Garzia L,
886 Gutmann DH, Hanahan D, Hervey-Jumper SL, Hondermarck H, Hurov JB, Kepecs A, Knox
887 SM, Lloyd AC, Magnon C, Saloman JL, Segal RA, Sloan EK, Sun X, Taylor MD, Tracey
888 KJ, Trotman LC, Tuveson DA, Wang TC, White RA, Winkler F. 2020. Roadmap for the
889 Emerging Field of Cancer Neuroscience. Cell. 181:219–222.

890 Murray E, Cho JH, Goodwin D, Ku T, Swaney J, Kim SY, Choi H, Park YG, Park JY,
891 Hubbert A, McCue M, Vassallo S, Bakh N, Frosch MP, Wedeen VJ, Seung HS, Chung K.
892 2015. Simple, Scalable Proteomic Imaging for High-Dimensional Profiling of Intact
893 Systems. Cell.

894 Neftel C, Laffy J, Filbin MG, Hara T, Shore ME, Rahme GJ, Richman AR, Silverbush D,
895 Shaw ML, Hebert CM, Dewitt J, Gritsch S, Perez EM, Gonzalez Castro LN, Lan X, Druck
896 N, Rodman C, Dionne D, Kaplan A, Bertalan MS, Small J, Pelton K, Becker S, Bonal D,
897 Nguyen Q De, Servis RL, Fung JM, Mylvaganam R, Mayr L, Gojo J, Haberler C,
898 Geyeregger R, Czech T, Slavc I, Nahed B V., Curry WT, Carter BS, Wakimoto H,
899 Brastianos PK, Batchelor TT, Stemmer-Rachamimov A, Martinez-Lage M, Frosch MP,
900 Stamenkovic I, Riggi N, Rheinbay E, Monje M, Rozenblatt-Rosen O, Cahill DP, Patel AP,
901 Hunter T, Verma IM, Ligon KL, Louis DN, Regev A, Bernstein BE, Tirosh I, Suvà ML. 2019.
902 An Integrative Model of Cellular States, Plasticity, and Genetics for Glioblastoma. Cell.
903 178:835-849.e21.

904 Ney PA. 2015. Mitochondrial autophagy: Origins, significance, and role of BNIP3 and NIX.
905 Biochim Biophys Acta Mol Cell Res.

906 Ogawa J, Pao GM, Shokhirev MN, Verma IM. 2018a. Glioblastoma Model Using Human
907 Cerebral Organoids. Cell Rep. 23:1220–1229.

908 Ogawa J, Pao GM, Shokhirev MN, Verma IM. 2018b. Glioblastoma Model Using Human
909 Cerebral Organoids. Cell Rep. 23:1220–1229.

910 Osswald M, Jung E, Sahm F, Solecki G, Venkataramani V, Blaes J, Weil S, Horstmann H,
911 Wiestler B, Syed M, Huang L, Ratliff M, Karimian Jazi K, Kurz FT, Schmenger T, Lemke D,
912 Gömmel M, Pauli M, Liao Y, Häring P, Pusch S, Herl V, Steinhäuser C, Krunic D, Jarahian
913 M, Miletic H, Berghoff AS, Griesbeck O, Kalamakis G, Garaschuk O, Preusser M, Weiss S,

914 Liu H, Heiland S, Platten M, Huber PE, Kuner T, Von Deimling A, Wick W, Winkler F. 2015.
915 Brain tumour cells interconnect to a functional and resistant network. Nature. 528:93–98.

916 Ostrom QT, Cioffi G, Gittleman H, Patil N, Waite K, Kruchko C, Barnholtz-Sloan JS. 2019.
917 CBTRUS Statistical Report: Primary Brain and Other Central Nervous System Tumors
918 Diagnosed in the United States in 2012-2016. Neuro Oncol. 21:V1–V100.

919 Pasca AM, Sloan SA, Clarke LE, Tian Y, Makinson CD, Huber N, Kim CH, Park JY,
920 O'Rourke NA, Nguyen KD, Smith SJ, Huguenard JR, Geschwind DH, Barres BA, Pasca
921 SP. 2015. Functional cortical neurons and astrocytes from human pluripotent stem cells in
922 3D culture. Nat Methods.

923 Patel AP, Tirosh I, Trombetta JJ, Shalek AK, Gillespie SM, Wakimoto H, Cahill DP, Nahed
924 B V., Curry WT, Martuza RL, Louis DN, Rozenblatt-Rosen O, Suvà ML, Regev A,
925 Bernstein BE. 2014. Single-cell RNA-seq highlights intratumoral heterogeneity in primary
926 glioblastoma. Science (1979). 344:1396–1401.

927 Pine AR, Cirigliano SM, Nicholson JG, Hu Y, Linkous A, Miyaguchi K, Edwards L,
928 Singhania R, Schwartz TH, Ramakrishna R, Pisapia DJ, Snuderl M, Elemento O, Fine HA.
929 2020a. Tumor microenvironment is critical for the maintenance of cellular states found in
930 primary glioblastomas. Cancer Discov. 10:964–979.

931 Pine AR, Cirigliano SM, Nicholson JG, Hu Y, Linkous A, Miyaguchi K, Edwards L,
932 Singhania R, Schwartz TH, Ramakrishna R, Pisapia DJ, Snuderl M, Elemento O, Fine HA.
933 2020b. Tumor microenvironment is critical for the maintenance of cellular states found in
934 primary glioblastomas. Cancer Discov. 10:964–979.

935 Pollen AA, Nowakowski TJ, Chen J, Retallack H, Sandoval-Espinosa C, Nicholas CR,
936 Shuga J, Liu SJ, Oldham MC, Diaz A, Lim DA, Leyrat AA, West JA, Kriegstein AR. 2015.
937 Molecular Identity of Human Outer Radial Glia during Cortical Development. Cell.

938 Qian X, Nguyen HN, Song MM, Hadiono C, Ogden SC, Hammack C, Yao B, Hamersky
939 GR, Jacob F, Zhong C, Yoon KJ, Jeang W, Lin L, Li Y, Thakor J, Berg DA, Zhang C, Kang
940 E, Chickering M, Nauen D, Ho CY, Wen Z, Christian KM, Shi PY, Maher BJ, Wu H, Jin P,
941 Tang H, Song H, Ming GL. 2016. Brain-Region-Specific Organoids Using Mini-bioreactors
942 for Modeling ZIKV Exposure. Cell.

943 Rakic P. 2009. Evolution of the neocortex: a perspective from developmental biology. Nat
944 Rev Neurosci. 10:724–735.

945 Sanai N, Alvarez-Buylla A, Berger MS. 2005. Neural Stem Cells and the Origin of Gliomas,
946 n engl j med.

947 Schlessinger J. 2000. Cell Signaling by Receptor Tyrosine Kinases, Cell.

948 Skaga E, Kulesskiy E, Fayzullin A, Sandberg CJ, Potdar S, Kyttälä A, Langmoen IA,
949 Laakso A, Gaál-Paavola E, Perola M, Wennerberg K, Vik-Mo EO. 2019. Intertumoral
950 heterogeneity in patient-specific drug sensitivities in treatment-naïve glioblastoma. BMC
951 Cancer. 19:1–14.

952 Sottoriva A, Spiteri I, Piccirillo SGM, Touloumis A, Collins VP, Marioni JC, Curtis C, Watts
953 C, Tavaré S. 2013. Intratumor heterogeneity in human glioblastoma reflects cancer
954 evolutionary dynamics. Proc Natl Acad Sci U S A. 110:4009–4014.

955 Squair JW, Gautier M, Kathe C, Anderson MA, James ND, Hutson TH, Hudelle R, Qaiser
956 T, Matson KJE, Barraud Q, Levine AJ, la Manno G, Skinnider MA, Courtine G. 2021.
957 Confronting false discoveries in single-cell differential expression. Nat Commun. 12.

958 Strickland M, Stoll EA. 2017. Metabolic reprogramming in glioma. Front Cell Dev Biol.

959 Sun X, Lin Y. 2016. Npas4: Linking Neuronal Activity to Memory. Trends Neurosci.

960 Szymczyk J, Sluzalska KD, Materla I, Opalinski L, Otlewski J, Zakrzewska M. 2021.
961 Fgf/fgfr-dependent molecular mechanisms underlying anti-cancer drug resistance. Cancers
962 (Basel). 13.

963 Tan AC, Ashley DM, López GY, Malinzak M, Friedman HS, Khasraw M. 2020.
964 Management of glioblastoma: State of the art and future directions. CA Cancer J Clin.
965 70:299–312.

966 Tang M, Xie Q, Gimple RC, Zhong Z, Tam T, Tian J, Kidwell RL, Wu Q, Prager BC, Qiu Z,
967 Yu A, Zhu Z, Mesci P, Jing H, Schimelman J, Wang P, Lee D, Lorenzini MH, Dixit D, Zhao
968 L, Bhargava S, Miller TE, Wan X, Tang J, Sun B, Cravatt BF, Muotri AR, Chen S, Rich JN.
969 2020. Three-dimensional bioprinted glioblastoma microenvironments model cellular
970 dependencies and immune interactions. Cell Res. 30:833–853.

971 Tejero R, Huang Y, Katsyv I, Kluge M, Lin JY, Tome-Garcia J, Daviaud N, Wang Y, Zhang
972 B, Tsankova NM, Friedel CC, Zou H, Friedel RH. 2019. Gene signatures of quiescent
973 glioblastoma cells reveal mesenchymal shift and interactions with niche microenvironment.
974 EBioMedicine. 42:252–269.

975 Tykocki T, Eltayeb M. 2018. Ten-year survival in glioblastoma. A systematic review.
976 Journal of Clinical Neuroscience.

977 Venkataramani V, Tanev DI, Strahle C, Studier-Fischer A, Fankhauser L, Kessler T, Körber
978 C, Kardorff M, Ratliff M, Xie R, Horstmann H, Messer M, Paik SP, Knabbe J, Sahm F, Kurz
979 FT, Acikgöz AA, Herrmannsdörfer F, Agarwal A, Bergles DE, Chalmers A, Miletic H,
980 Turcan S, Mawrin C, Hänggi D, Liu HK, Wick W, Winkler F, Kuner T. 2019. Glutamatergic
981 synaptic input to glioma cells drives brain tumour progression. Nature. 573:532–538.

982 Venkataramani V, Yang Y, Schubert MC, Reyhan E, Tetzlaff SK, Wißmann N, Botz M,
983 Soyka SJ, Beretta CA, Pramatarov R, Fankhauser L, Garofano L, Freudenberg A, Wagner
984 J, Tanev DI, Ratliff M, Xie R, Kessler T, Hoffmann DC, Hai L, Dörflinger Y, Hoppe S, Yabo
985 Y, Golebiewska A, Niclou S, Lasorella A, Slowik M, Döring L, Iavarone A, Wick W, Kuner T,
986 Winkler F. 2022. Glioblastoma hijacks neuronal mechanisms for brain invasion. Cell. 2899–
987 2917.

988 Venkatesh HS, Johung TB, Caretti V, Noll A, Tang Y, Nagaraja S, Gibson EM, Mount CW,
989 Polepalli J, Mitra SS, Woo PJ, Malenka RC, Vogel H, Bredel M, Mallick P, Monje M. 2015.
990 Neuronal activity promotes glioma growth through neuroligin-3 secretion. Cell. 161:803–
991 816.

992 Venkatesh HS, Morishita W, Geraghty AC, Silverbush D, Gillespie SM, Arzt M, Tam LT,
993 Espenel C, Ponnuswami A, Ni L, Woo PJ, Taylor KR, Agarwal A, Regev A, Brang D, Vogel
994 H, Hervey-Jumper S, Bergles DE, Suvà ML, Malenka RC, Monje M. 2019. Electrical and
995 synaptic integration of glioma into neural circuits. Nature. 573:539–545.

996 Venkatesh HS, Tam LT, Woo PJ, Lennon J, Nagaraja S, Gillespie SM, Ni J, Duveau DY,
997 Morris PJ, Zhao JJ, Thomas CJ, Monje M. 2017. Targeting neuronal activity-regulated
998 neuroligin-3 dependency in high-grade glioma. Nature. 549:533–537.

999 Wang Q, Hu B, Hu X, Kim H, Squatrito M, Scarpace L, deCarvalho AC, Lyu S, Li P, Li Y,
1000 Barthel F, Cho HJ, Lin YH, Satani N, Martinez-Ledesma E, Zheng S, Chang E, Gabriel
1001 Sauvé CE, Olar A, Lan ZD, Finocchiaro G, Phillips JJ, Berger MS, Gabrusiewicz KR, Wang
1002 G, Eskilsson E, Hu J, Mikkelsen T, DePinho RA, Muller F, Heimberger AB, Sulman EP,

1003 Nam DH, Verhaak RGW. 2018. Tumor Evolution of Glioma-Intrinsic Gene Expression
1004 Subtypes Associates with Immunological Changes in the Microenvironment. Cancer Cell.
1005 33:152.

1006 Wang Y, Chiola S, Yang G, Russell C, Armstrong CJ, Wu Y, Spampanato J, Tarboton P,
1007 Ullah HMA, Edgar NU, Chang AN, Harmin DA, Bocchi VD, Vezzoli E, Besusso D, Cui J,
1008 Cattaneo E, Kubanek J, Shcheglovitov A. 2022. Modeling human telencephalic
1009 development and autism-associated SHANK3 deficiency using organoids generated from
1010 single neural rosettes. Nat Commun. 13.

1011 Watanabe M, Buth JE, Vishlaghi N, de la Torre-Ubieta L, Taxidis J, Khakh BS, Coppola G,
1012 Pearson CA, Yamauchi K, Gong D, Dai X, Damoiseaux R, Aliyari R, Liebscher S, Schenke-
1013 Layland K, Caneda C, Huang EJ, Zhang Y, Cheng G, Geschwind DH, Golshani P, Sun R,
1014 Novitch BG. 2017. Self-Organized Cerebral Organoids with Human-Specific Features
1015 Predict Effective Drugs to Combat Zika Virus Infection. Cell Rep. 21:517–532.

1016 Wenger A, Vega SF, Kling T, Bontell TO, Jakola AS, Carén H. 2019. Intratumor DNA
1017 methylation heterogeneity in glioblastoma: Implications for DNA methylation-based
1018 classification. Neuro Oncol. 21:616–627.

1019 Xie XP, Laks DR, Sun D, Ganbold M, Wang Z, Pedraza AM, Bale T, Tabar V, Brennan C,
1020 Zhou X, Parada LF. 2022. Quiescent human glioblastoma cancer stem cells drive tumor
1021 initiation, expansion, and recurrence following chemotherapy. Dev Cell. 57:32-46.e8.

1022 Xu J, Zhang G, Hu J, Li H, Zhao J, Zong S, Guo Z, Jiang Y, Jing Z. 2022.
1023 UPF1/circRPPH1/ATF3 feedback loop promotes the malignant phenotype and stemness of
1024 GSCs. Cell Death Dis. 13.

1025 Yabo YA, Niclou SP, Golebiewska A. 2022. Cancer cell heterogeneity and plasticity: A
1026 paradigm shift in glioblastoma. Neuro Oncol. 24:669–682.

1027 Ye C, Li H, Li Y, Zhang Y, Liu G, Mi H, Li H, Xiao Q, Niu L, Yu X. 2022. Hypoxia-induced
1028 HMGB1 promotes glioma stem cells self-renewal and tumorigenicity via RAGE. iScience.
1029 25.

1030 Yu K, Lin CCJ, Hatcher A, Lozzi B, Kong K, Huang-Hobbs E, Cheng YT, Beechar VB, Zhu
1031 W, Zhang Y, Chen F, Mills GB, Mohila CA, Creighton CJ, Noebels JL, Scott KL, Deneen B.
1032 2020. PIK3CA variants selectively initiate brain hyperactivity during gliomagenesis. Nature.
1033 578:166–171.

1034 Zhou Y, Zhou Y, Shingu T, Feng L, Chen Z, Ogasawara M, Keating MJ, Kondo S, Huang
1035 P. 2011. Metabolic alterations in highly tumorigenic glioblastoma cells: Preference for
1036 hypoxia and high dependency on glycolysis. Journal of Biological Chemistry. 286:32843–
1037 32853.

1038

642 **FIGURE LEGENDS**

643 **Figure 1. A-B** Schematics of the pipeline for the derivation, different culturing conditions
644 and single-cell profiling of GBM11 (PN) and GBM20 (MS) GBMs. **C-D** Images of GBM11
645 (C) and GBM20 (D) spheroids grown in presence (left) or absence (right) of exogenous
646 EGF-FGF supplementation. **E-F** Growth curves for GBM11 (E) and GBM20 (F) spheroids
647 with or without EGF/FGF. **G** UMAP plot of clusters from GBM20 and GBM11 cells in
648 spheroids. **H** UMAP plot of Seurat clusters. **I** Bar plot showing the cluster composition of
649 PN and MS tumors in spheroids. Stacked bars show the proportional composition for each
650 tumor. **J** Similarity matrix of clusters from GBM11 and GBM20 tumor cells. Heatmap color
651 indicates the Spearman ranked correlation. **K** Feature plots for selected PN, MES and
652 cancer stem cell genes in spheroids. **L** Pie charts of percentages of cells in spheroids
653 classified as astrocytic (AC)-like, mesenchymal (MES)-like, neural-progenitor (NPC)-like,
654 and oligodendrocyte-progenitor (OPC)-like states. Scale bars: 500 μm (C-D). Data are
655 presented as mean ± standard error of the mean (s.e.m.).

656

657 **Figure 2. A** Images of SNR-derived subpallial organoids at 2, 7, and 14 days in vitro post-
658 isolation. **B** Scatter plot sized of organoids produced from iPSC-RFP and H9 stem cell
659 lines in 3 (2 iPSC, combined and 1 H9) independent differentiation batches. Each dot
660 represents an organoid. **C** UMAP plots of cells collected from multiple organoids obtained
661 in 3 different differentiation batches from iPSC-RFP and H9 stem cell lines. **D** UMAP plot
662 of Seurat clusters. **E** Bar plot showing cell cluster compositions for 3 different
663 differentiation batches. **F** Similarity gene expression matrix for different cell clusters (IPs:
664 intermediate progenitors; NPs: neural progenitors). **G** Feature heat-map plots for selected

665 pallial and subpallial cell type-specific markers. **H** Dot plot for pallial and subpallial cell
666 type-specific markers. Scale bar: 250 μm (A).
667
668 **Figure 3**. **A** Schematics of the experimental design for the generation of fused GBM
669 spheroids and subpallial organoids (organoids-GBM chimeras). **B** Images of GBM20-
670 iPSC chimeras at weeks 1, 2, and 3 post fusion. **C** Images of cleared MS-GBM-iPSC
671 chimera. **D** Images of MS-GBM-iPSC chimera. **E** UMAP plot of Seurat clusters. **F** UMAP
672 plot of cells coming from 5 independent groups of chimeras from 3 distinct batches. **G** Bar
673 plot showing percentages of cell clusters in MS- and PN-chimeras. **H** Similarity matrix of
674 clusters from chimeras. **I** Pie charts of percentages of tumor cells in MS- and PN-chimeras
675 classified as AC-like, MES-like, NPC-like, and OPC-like states. **J** Violin plots of gene
676 expression for selected MS and PN genes in tumor cells from chimeras and spheroids.
677 Scale bar: 200 μm (B-D). Benjamini and Hochberg FDR: *<0.05, **<0.01.
678
679 **Figure 4**. **A** Scheme of the differential expression analysis workflow. **B-C** UMAP plot of
680 cells coming from tumors clustered by origin (chimeras or spheroids [B]) or tumor type
681 (C). **D** UMAP plot of clusters from combined tumor cells coming from Chimeras and
682 spheroids, colored by cluster. **E** Similarity matrix of clusters from combined analysis.
683 Heatmap color indicates the Spearman ranked correlation, and above the heatmap is the
684 annotated “grouped cluster” for each cluster. **F** UMAP plot of “grouped clusters”. **G** Bar
685 plot showing the cluster composition of PN and MS tumors in Chimeras and spheroids.
686 **H** Volcano plot of differentially expressed genes shows the most up- and down-regulated
687 genes found in PN tumor cells in Chimeras versus spheroids (left). Gene sets significantly

688 enriched (pvalue < 0.05) in the PN tumor grown in Chimeras using the Gene Ontology
689 Biological Processes, ordered by NES [Normalized Enrichment Score] (right). A positive
690 NES indicates enrichment in the PN tumor grown in Chimeras, a negative NES indicates
691 enrichment in the PN tumor grown in spheroids. **I** Volcano plot of differentially expressed
692 genes shows the most up- and down-regulated genes found in MS tumor cells in
693 Chimeras versus spheroids (left). Gene sets significantly enriched (pvalue < 0.05) in the
694 MS tumor grown in Chimeras using the Gene Ontology Biological Processes, ordered by
695 NES (right). **J** Venn diagram showing the number of common (list on the right) and unique
696 upregulated genes (adjusted pvalue < 0.05, logFC > 0.25) in PN and MS tumors in
697 Chimeras. **K** Venn diagram showing the number of common (list on the right) and unique
698 down-regulated genes (adjusted pvalue < 0.05, logFC < -0.25) in PN and MS tumors in
699 Chimeras. **L-N** Heat maps of the "mitosis", "s-phase", and "cancer stem cell" gene
700 signatures for PN and MS tumors grown in spheroids and chimeras.
701
702 **Figure 5**. **A** Schematics for the differential expression analysis design. B UMAP plot of
703 cells coming from organoids clustered by origin (organoids or chimeras, left) or sample
704 name (right). C UMAP plot of Seurat clusters. D Similarity matrix of clusters from
705 organoids and organoids in chimeras (MS and PN). E Bar plot showing the percentages
706 of clusters in different batches of organoids and organoids in chimeras (MS and PN). F
707 Dot plot for pallial and subpallial specific markers in organoids' clusters. **G-H** Principal
708 Component Analysis (PCA) plots of pseudo bulk RNA seq values for Neural Progenitors
709 (G) and Neurons (H) in organoids and chimeras. **I** Volcano plot of differentially expressed
710 genes shows the most up- and down-regulated genes found in Neuronal cells in Chimeras

711 versus Organoids (left). Gene sets significantly enriched (pvalue < 0.05) in Neurons in
712 Chimeras using the Gene Ontology Biological Processes, ordered by NES (right). **J**
713 Volcano plot of differentially expressed genes shows the most up- and down-regulated
714 genes found in Neural Progenitor cells in Chimeras versus Organoids (left). Gene sets
715 significantly enriched (pvalue < 0.05) in Neural Progenitors in Chimeras using the Gene
716 Ontology Biological Processes, ordered by NES (right).
717
718
719
720
721
722
723
724
725
726
727
728
729
730
731
732
733

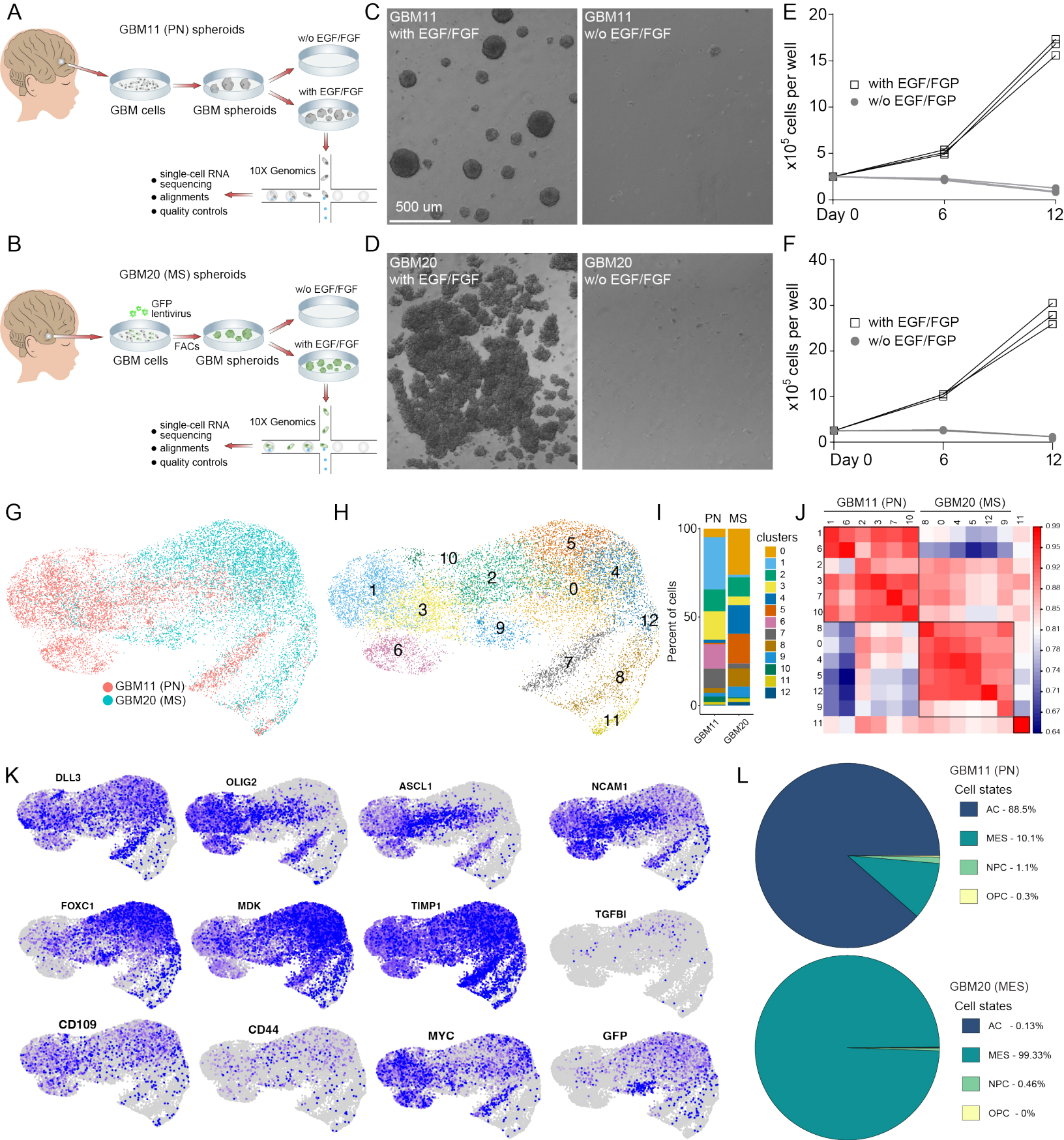
A
GBM11 (PN) spheroids
w/o EGF/FGF
with EGF/FGF
GBM cells
GBM spheroids
10X Genomics
single-cell RNA sequencing
alignments
quality controls
B
GBM20 (MS) spheroids
GFP lentivirus
FACs
C
GBM11 with EGF/FGF
GBM11 w/o EGF/FGF
500 um
D
GBM20 with EGF/FGF
GBM20 w/o EGF/FGF
E
x10^5 cells per well
with EGF/FGP
w/o EGF/FGP
Day 0
6
12
F
G
GBM11 (PN)
GBM20 (MS)
H
I
PN
MS
Percent of cells
clusters
GBM11
GBM20
J
GBM11 (PN)
GBM20 (MS)
K
DLL3
OLIG2
ASCL1
NCAM1
FOXC1
MDK
TIMP1
TGFBI
CD109
CD44
MYC
GFP
L
GBM11 (PN)
Cell states
AC - 88.5%
MES - 10.1%
NPC - 1.1%
OPC - 0.3%
GBM20 (MES)
Cell states
AC - 0.13%
MES - 99.33%
NPC - 0.46%
OPC - 0%

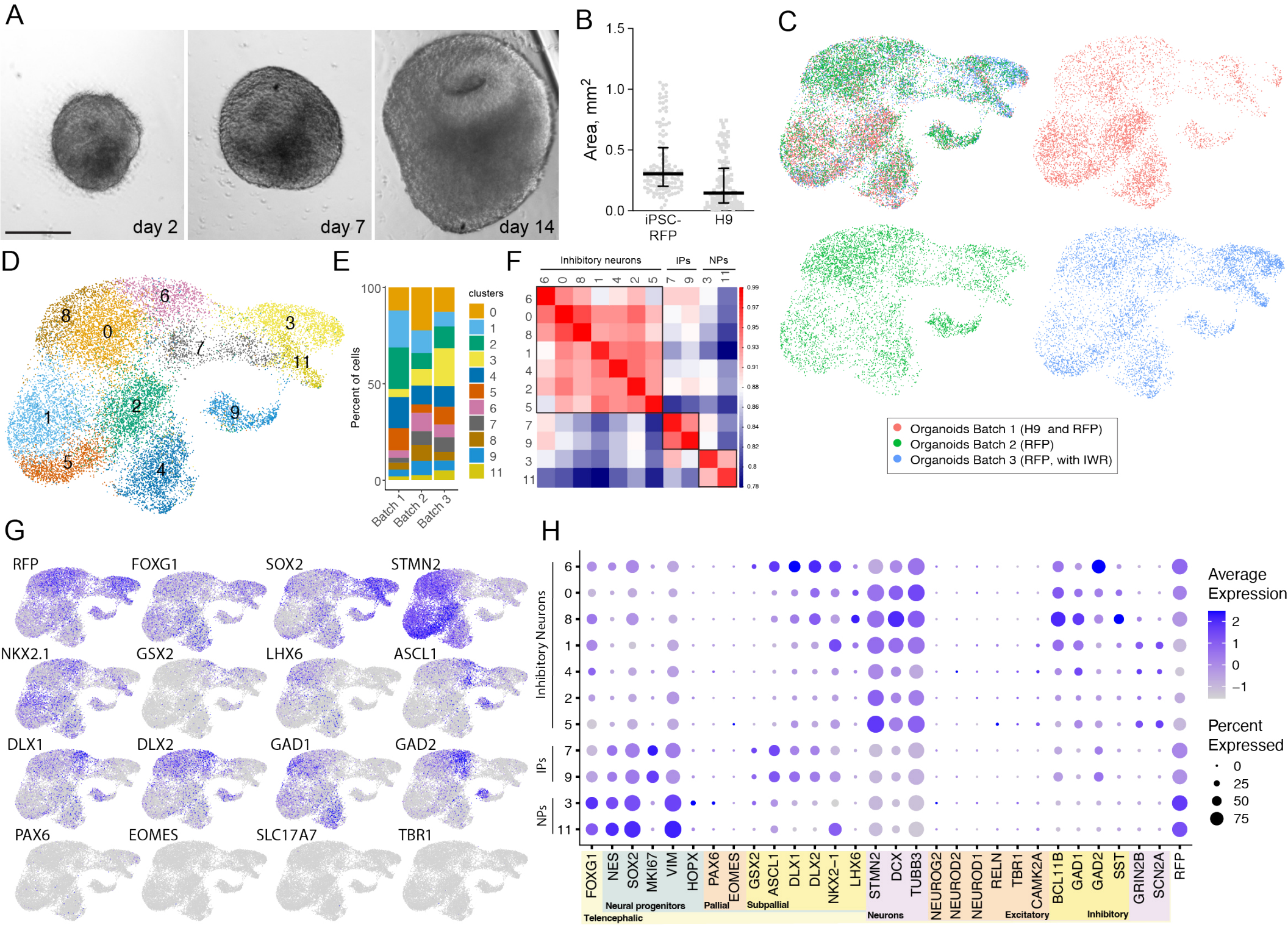
A
day 2
day 7
day 14
B
Area, mm2
1.5
1.0
0.5
0.0
iPSC-RFP
H9
C
Organoids Batch 1 (H9 and RFP)
Organoids Batch 2 (RFP)
Organoids Batch 3 (RFP, with IWR)
D
E
Percent of cells
100
50
0
Batch 1
Batch 2
Batch 3
clusters
F
Inhibitory neurons
IPs
NPs
G
RFP
FOXG1
SOX2
STMN2
NKX2.1
GSX2
LHX6
ASCL1
DLX1
DLX2
GAD1
GAD2
PAX6
EOMES
SLC17A7
TBR1
H
Inhibitory Neurons
IPs
NPs
Average Expression
Percent Expressed
FOXG1
NES
SOX2
MKI67
VIM
HOPX
PAX6
EOMES
GSX2
ASCL1
DLX1
DLX2
NKX2-1
LHX6
STMN2
DCX
TUBB3
NEUROG2
NEUROD2
NEUROD1
RELN
TBR1
CAMK2A
BCL11B
GAD1
GAD2
SST
GRIN2B
SCN2A
RFP
Neural progenitors
Pallial
Subpallial
Telencephalic
Neurons
Excitatory
Inhibitory

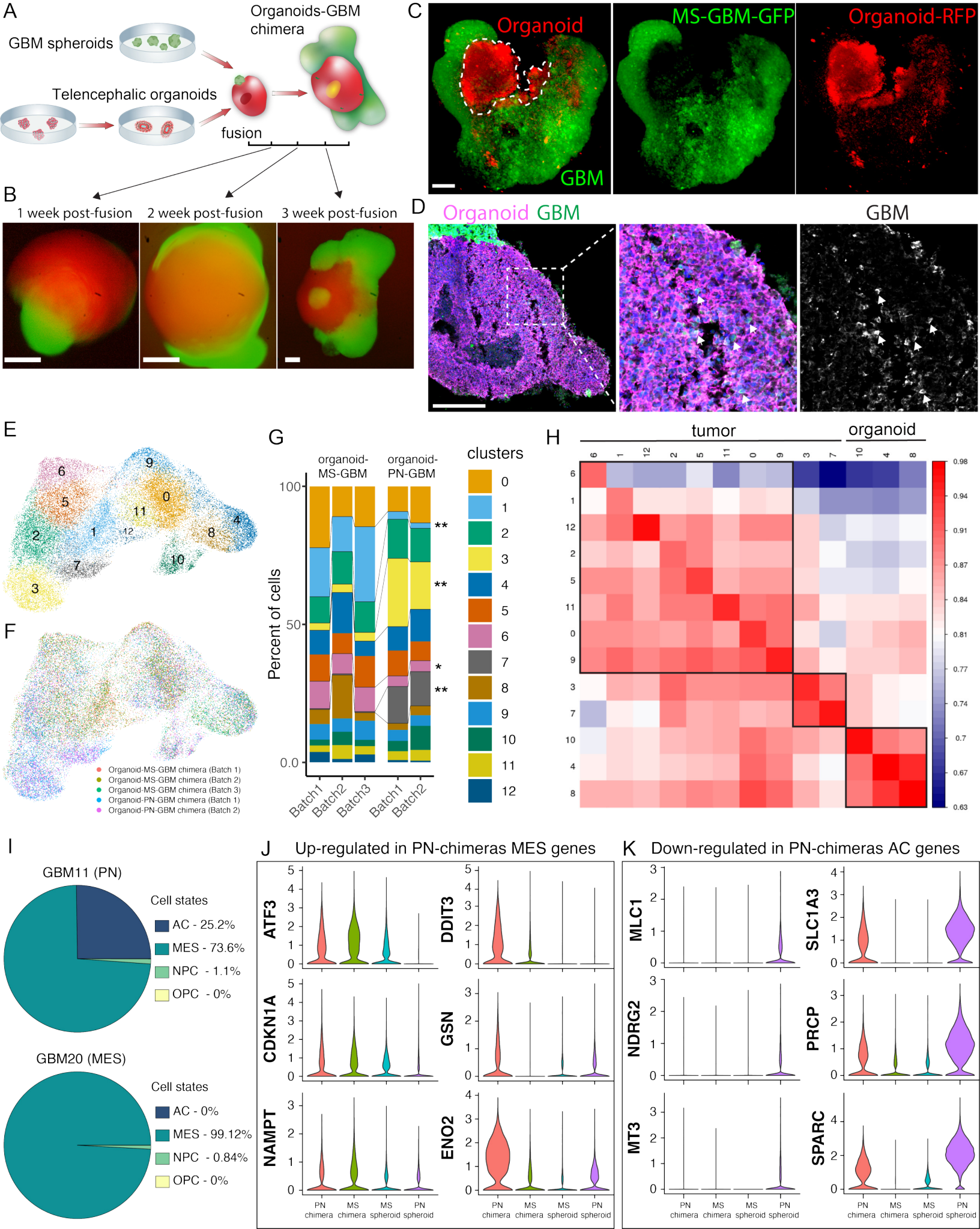
A
GBM spheroids
Organoids-GBM chimera
Telencephalic organoids
fusion
B
1 week post-fusion
2 week post-fusion
3 week post-fusion
C
Organoid
GBM
MS-GBM-GFP
Organoid-RFP
D
Organoid GBM
GBM
E
F
Organoid-MS-GBM chimera (Batch 1)
Organoid-MS-GBM chimera (Batch 2)
Organoid-MS-GBM chimera (Batch 3)
Organoid-PN-GBM chimera (Batch 1)
Organoid-PN-GBM chimera (Batch 2)
G
organoid-MS-GBM
organoid-PN-GBM
Percent of cells
Batch1
Batch2
Batch3
clusters
H
tumor
organoid
I
GBM11 (PN)
Cell states
AC - 25.2%
MES - 73.6%
NPC - 1.1%
OPC - 0%
GBM20 (MES)
AC - 0%
MES - 99.12%
NPC - 0.84%
OPC - 0%
J
Up-regulated in PN-chimeras MES genes
ATF3
DDIT3
CDKN1A
GSN
NAMPT
ENO2
PN chimera
MS chimera
MS spheroid
PN spheroid
K
Down-regulated in PN-chimeras AC genes
MLC1
SLC1A3
NDRG2
PRCP
MT3
SPARC

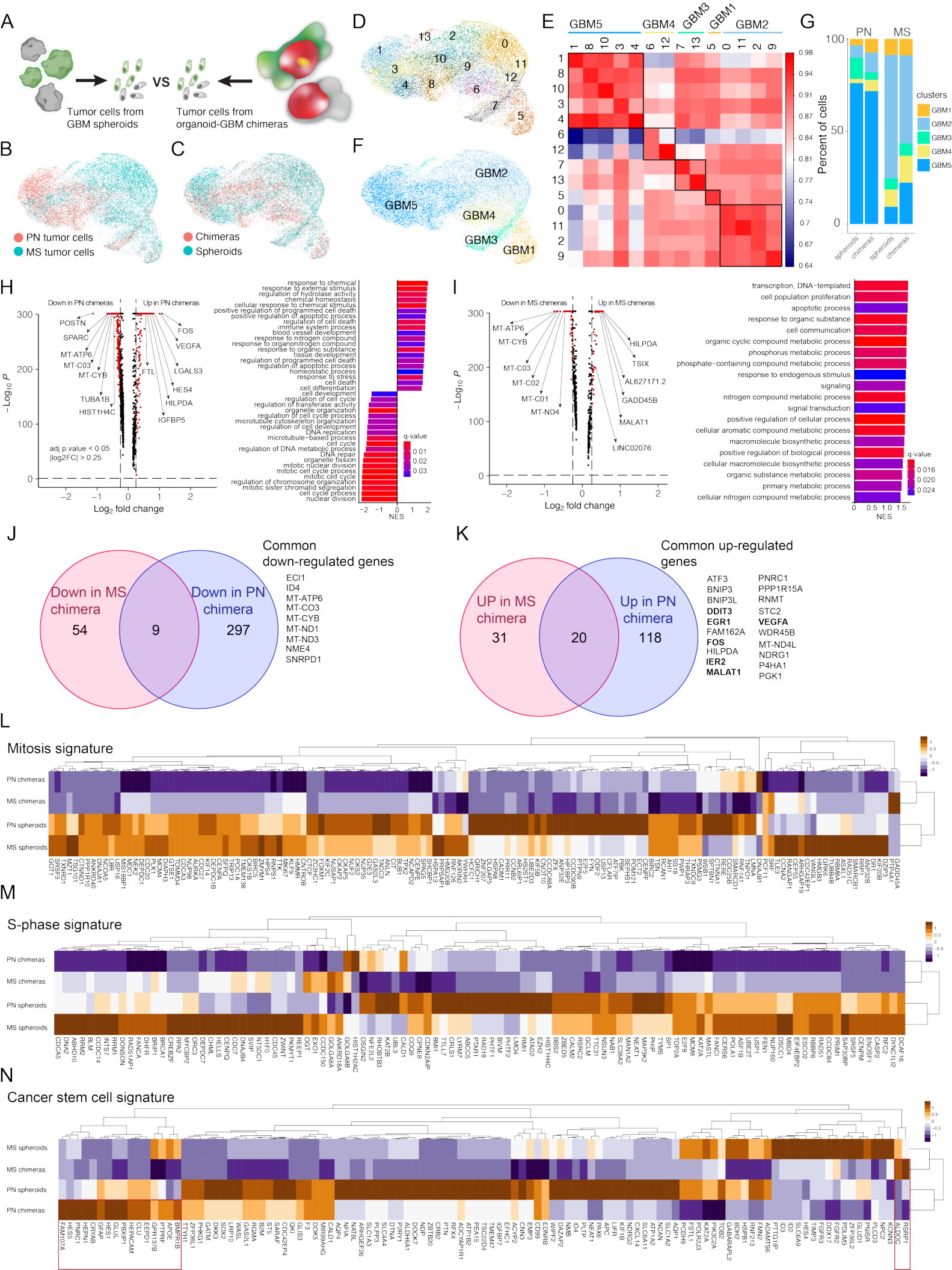
A
Tumor cells from GBM spheroids
vs
Tumor cells from organoid-GBM chimeras
B
PN tumor cells
MS tumor cells
C
Chimeras
Spheroids
D
E
GBM5
GBM4
GBM3
GBM1
GBM2
F
G
PN
MS
Percent of cells
clusters
H
Down in PN chimeras
Up in PN chimeras
POSTN
SPARC
MT-ATP6
MT-C03
MT-CYB
TUBA1B
HIST1H4C
FTL
FOS
VEGFA
LGALS3
HES4
HILPDA
IGFBP5
adj p value < 0.05
|log2FC| > 0.25
Log2 fold change
q-value
NES
I
Down in MS chimeras
Up in MS chimeras
MT-ATP6
MT-CYB
MT-C03
MT-C02
MT-C01
MT-ND4
HILPDA
TSIX
AL627171.2
GADD45B
MALAT1
LINC02076
Log2 fold change
J
Common down-regulated genes
Down in MS chimera
54
9
Down in PN chimera
297
ECI1
ID4
MT-ATP6
MT-CO3
MT-CYB
MT-ND1
MT-ND3
NME4
SNRPD1
K
Common up-regulated genes
UP in MS chimera
31
20
Up in PN chimera
118
ATF3
BNIP3
BNIP3L
DDIT3
EGR1
FAM162A
FOS
HILPDA
IER2
MALAT1
PNRC1
PPP1R15A
RNMT
STC2
VEGFA
WDR45B
MT-ND4L
NDRG1
P4HA1
PGK1
L
Mitosis signature
PN chimeras
MS chimeras
PN spheroids
MS spheroids
M
S-phase signature
PN chimeras
MS chimeras
PN spheroids
MS spheroids
N
Cancer stem cell signature
MS spheroids
MS chimeras
PN spheroids
PN chimeras

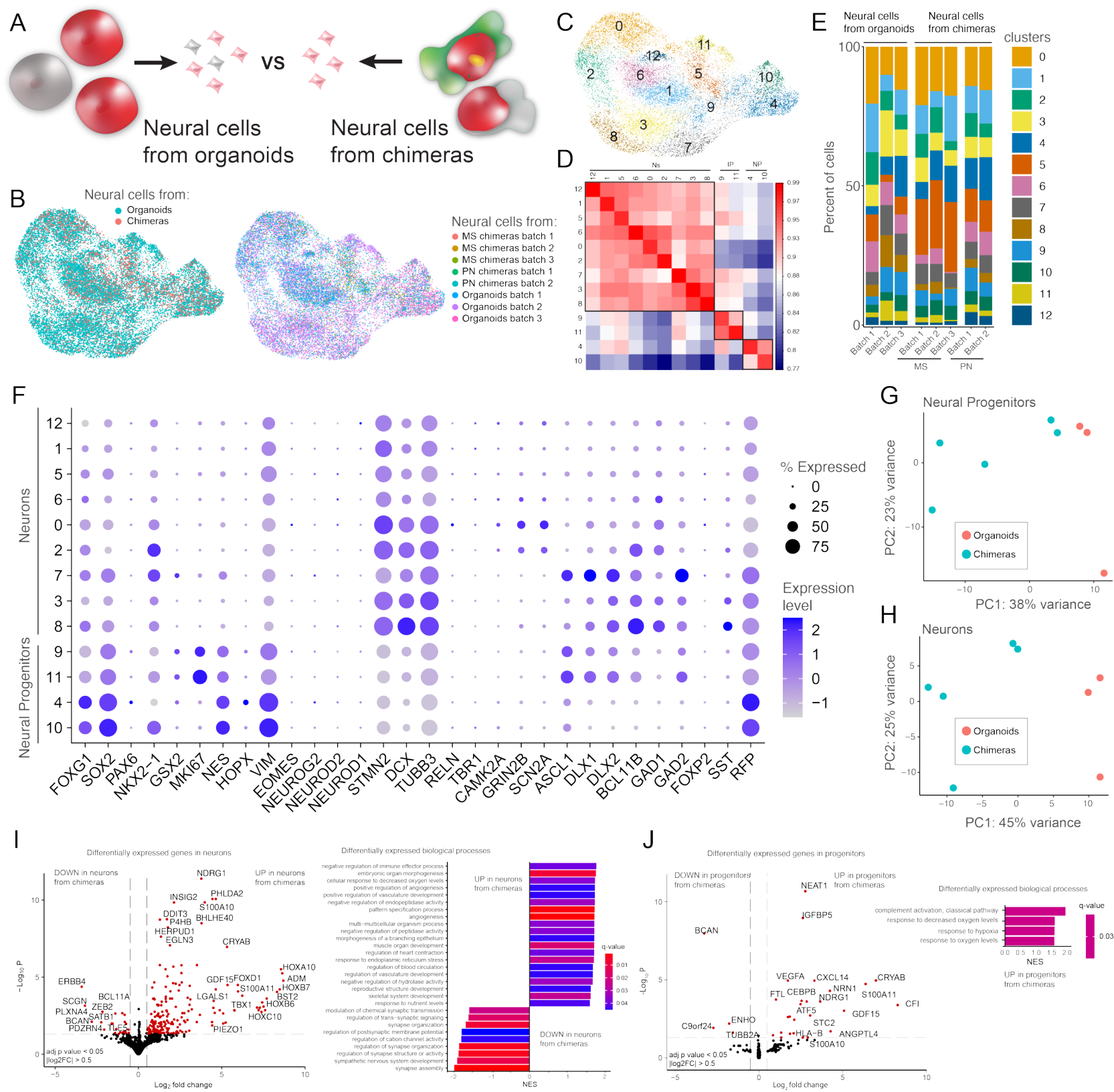
A
vs
Neural cells from organoids
Neural cells from chimeras
B
Neural cells from:
Organoids
Chimeras
Neural cells from:
MS chimeras batch 1
MS chimeras batch 2
MS chimeras batch 3
PN chimeras batch 1
PN chimeras batch 2
Organoids batch 1
Organoids batch 2
Organoids batch 3
C
D
Ns
IP
NP
E
Neural cells from organoids
Neural cells from chimeras
clusters
Percent of cells
Batch 1
Batch 2
Batch 3
MS
PN
F
Neurons
Neural Progenitors
% Expressed
Expression level
FOXG1
SOX2
PAX6
NKX2-1
GSX2
MKI67
NES
HOPX
VIM
EOMES
NEUROG2
NEUROD2
NEUROD1
STMN2
DCX
TUBB3
RELN
TBR1
CAMK2A
GRIN2B
SCN2A
ASCL1
DLX1
DLX2
BCL11B
GAD1
GAD2
FOXP2
SST
RFP
G
Neural Progenitors
PC2: 23% variance
PC1: 38% variance
Organoids
Chimeras
H
Neurons
PC2: 25% variance
PC1: 45% variance
Organoids
Chimeras
I
Differentially expressed genes in neurons
DOWN in neurons from chimeras
UP in neurons from chimeras
adj p value < 0.05
|log2FC| > 0.5
Log2 fold change
Differentially expressed biological processes
UP in neurons from chimeras
DOWN in neurons from chimeras
q-value
NES
J
Differentially expressed genes in progenitors
DOWN in progenitors from chimeras
UP in progenitors from chimeras
adj p value < 0.05
|log2FC| > 0.5
Log2 fold change
Differentially expressed biological processes
complement activation, classical pathway
response to decreased oxygen levels
response to hypoxia
response to oxygen levels
q-value
NES
UP in progenitors from chimeras

Supplementary Figures

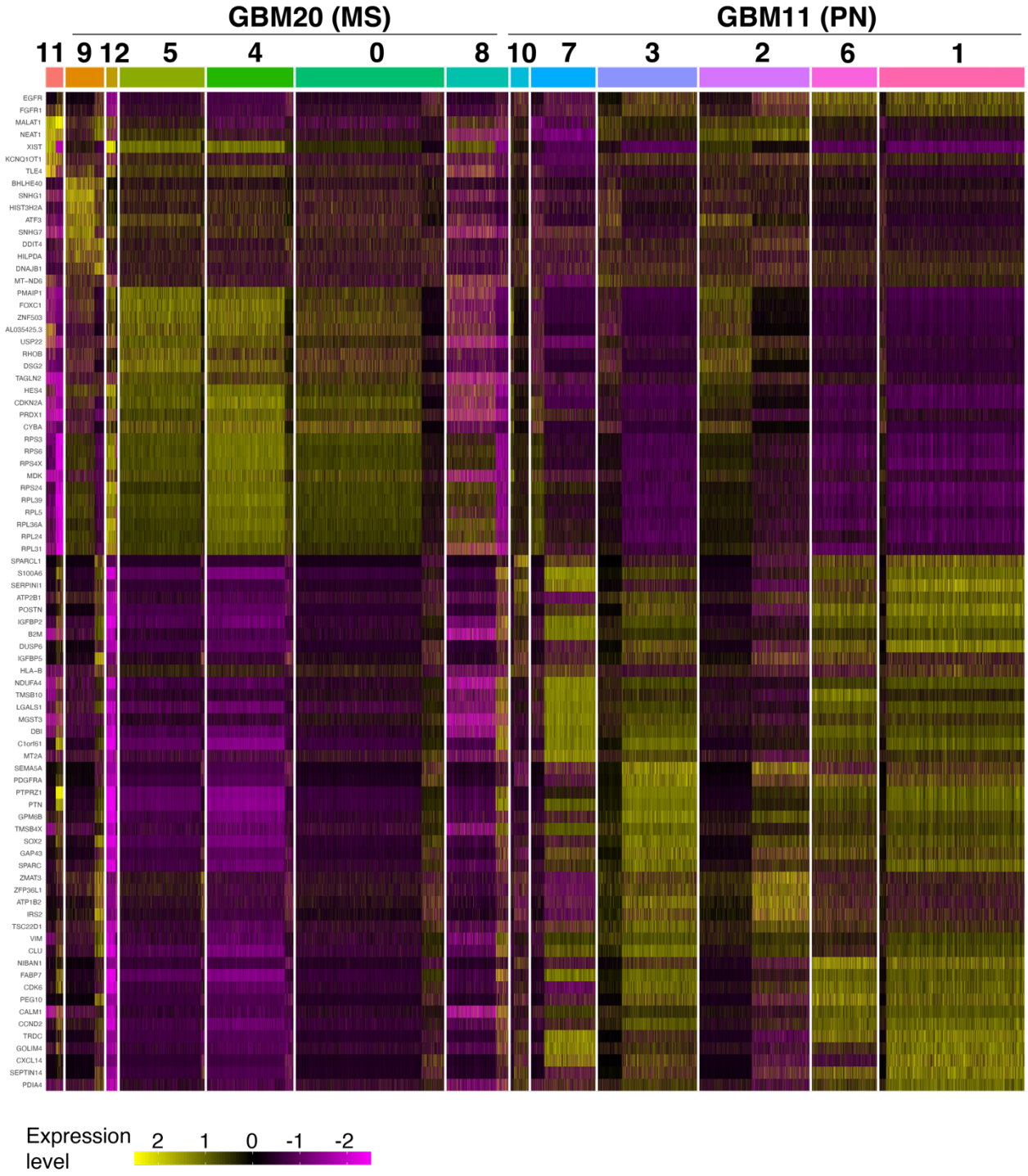

Supplementary Figure 1. Heatmap of cluster-specific genes calculated in Seurat clusters from PN (GBM11) and MS (GBM20) spheroids.

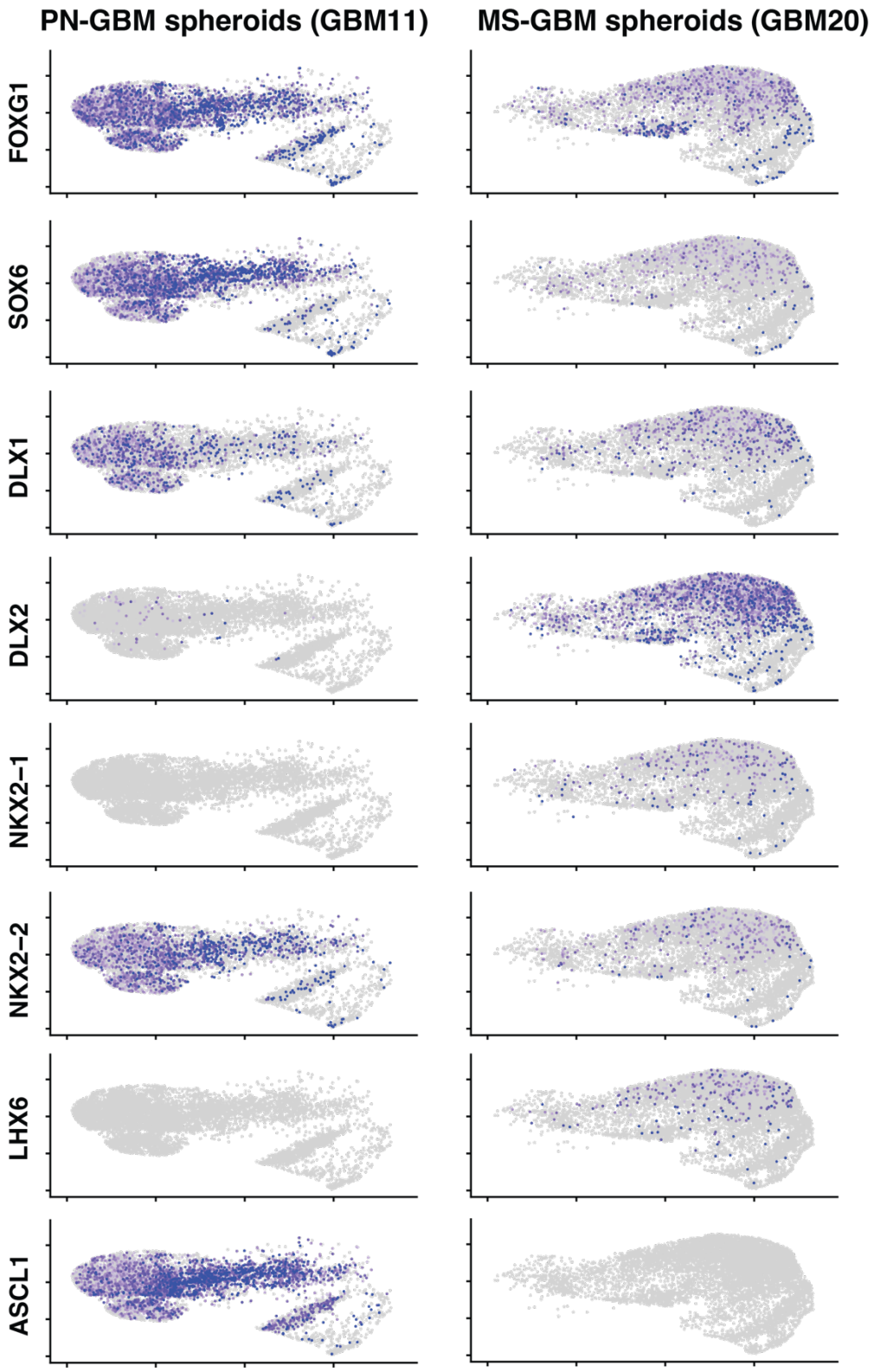

Supplementary Figure 2. Feature plots of expression levels for canonical subpallial markers in PN (GBM11) and MS (GBM20) spheroids.

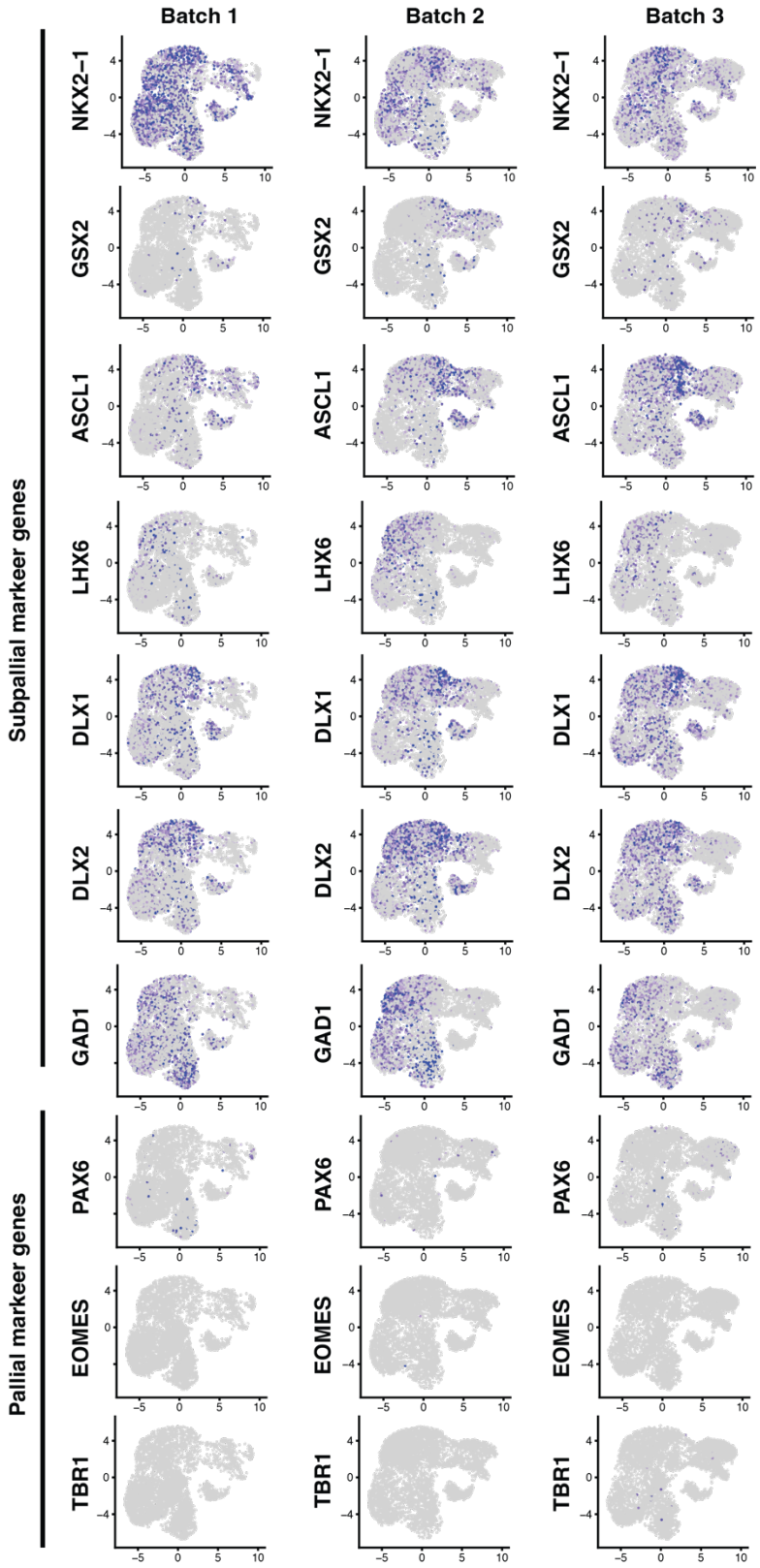

Supplementary Figure 3. Feature plots of expression levels for pallial and subpallial marker genes in 3 independent batches of SNR-derived organoids.

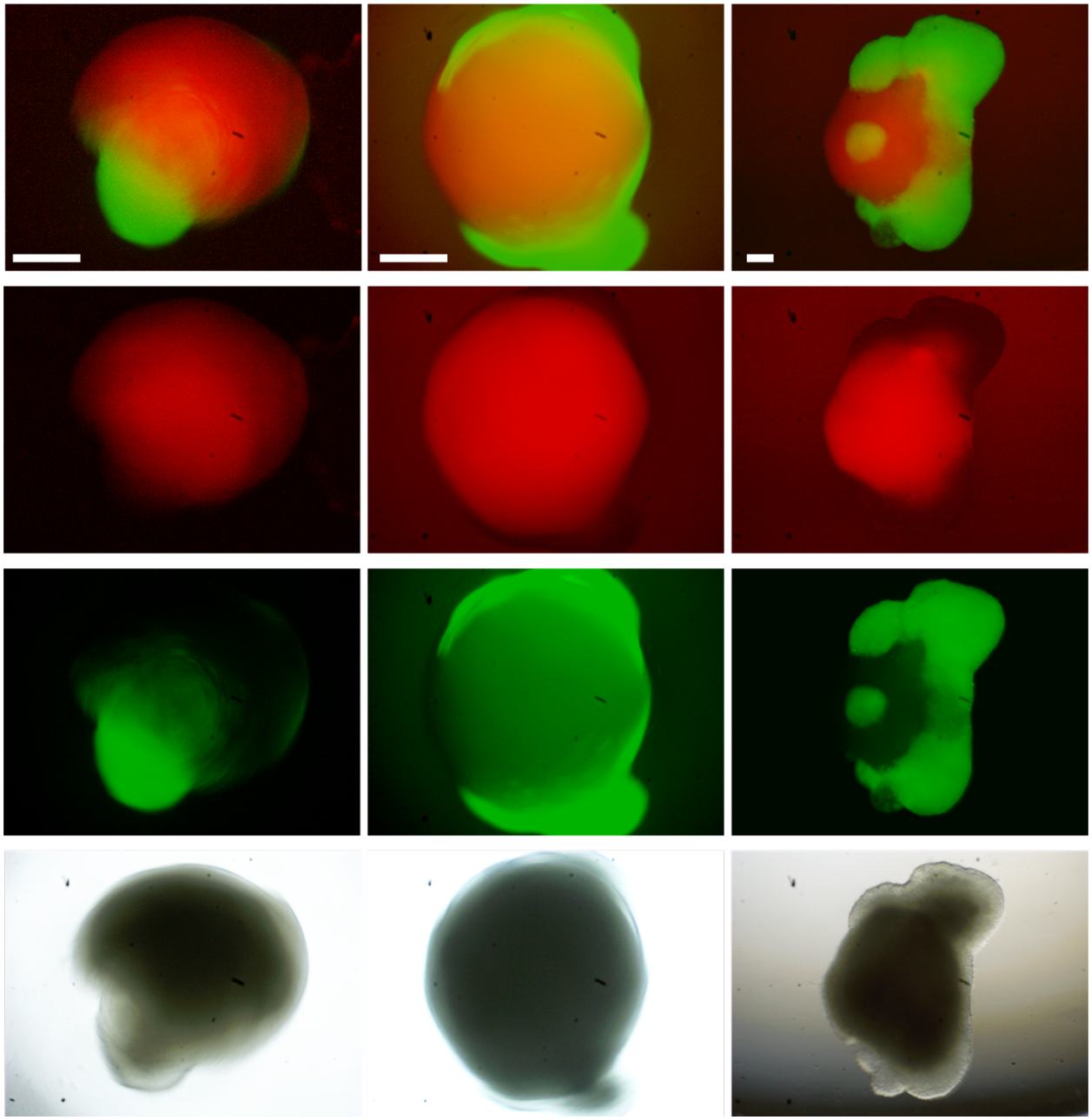

Supplementary Figure 4. Images of iPSC-RFP-derived-organoids-MS-GBM chimeras. Fluorescent (organoid:red, GBM:green) images are on the top rows, and bright field images are on the bottom row.

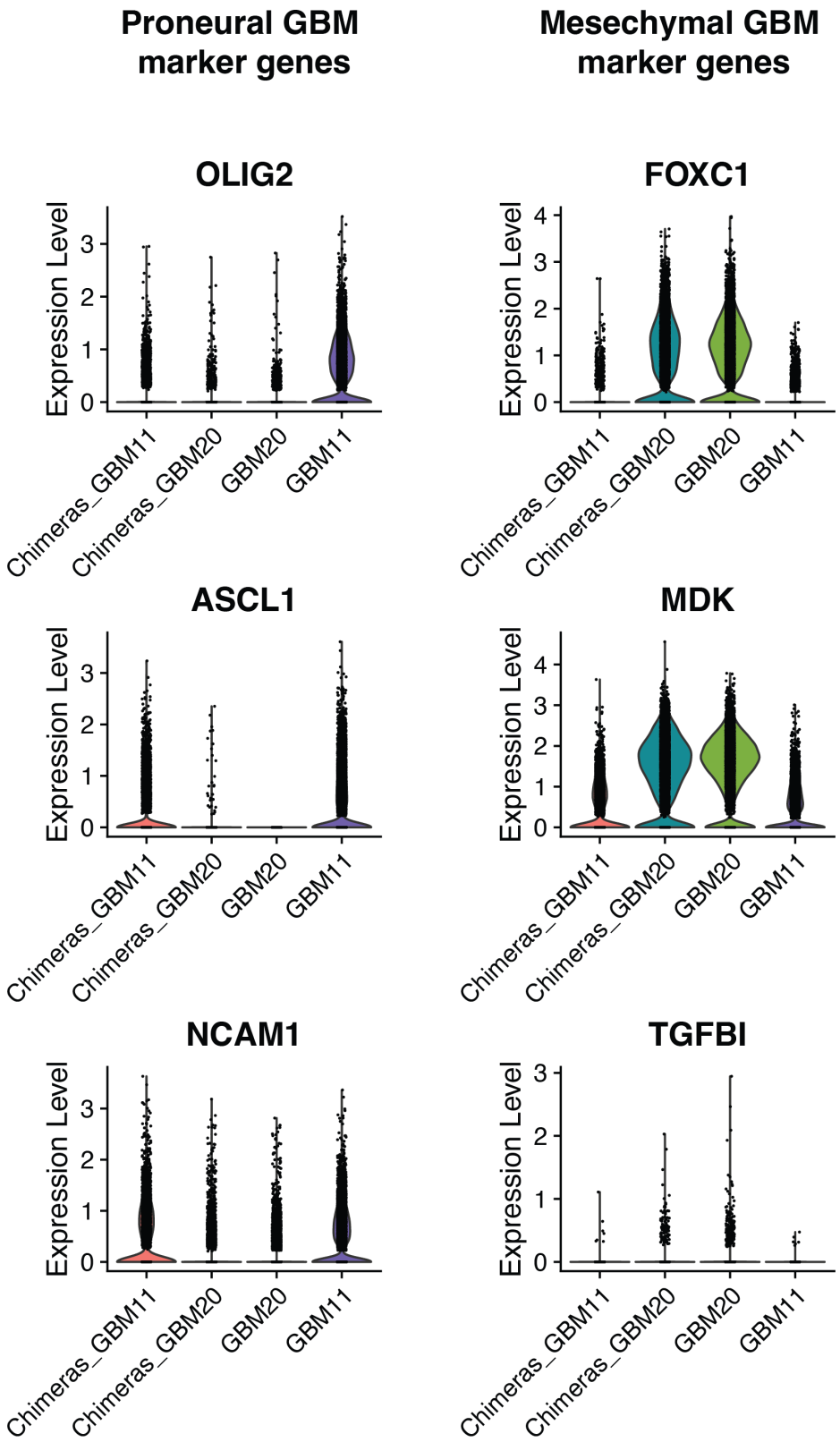

Supplementary Figure 5. Violin plot of selected PN and MS markers in tumor cells from PN (GBM11) and MS (GBM20) spheroids and chimeras.